Fermionic quantum criticality in honeycomb and π-flux Hubbard models: Finite-size scaling of renormalization-group-invariant observables from quantum Monte Carlo

Francesco Parisen Toldin, Martin Hohenadler, and Fakher F. Assaad

Institut für Theoretische Physik und Astrophysik, Universität Würzburg, Am Hubland, D-97074 Würzburg, Germany

Igor F. Herbut

Department of Physics, Simon Fraser University, Burnaby, British Columbia V5A 1S6, Canada

We numerically investigate the critical behavior of the Hubbard model on the honeycomb and the π-flux lattice, which exhibits a direct transition from a Dirac semimetal to an antiferromagnetically ordered Mott insulator. We use projective auxiliary-field quantum Monte Carlo simulations and a careful finite-size scaling analysis that exploits approximately improved renormalization-group-invariant observables. This approach, which is successfully verified for the three-dimensional XY transition of the Kane-Mele-Hubbard model, allows us to extract estimates for the critical couplings and the critical exponents. The results confirm that the critical behavior for the semimetal to Mott insulator transition in the Hubbard model belongs to the Gross-Neveu-Heisenberg universality class on both lattices.

I. INTRODUCTION

Understanding quantum phase transitions in which the order parameter couples to gapless fermions is an old and notorious problem in condensed matter theory [1]. In spite of recent advances (see, e.g., Refs. [2, 3]), the transitions in electronic systems with a full Fermi surface often elude controlled theoretical approaches. It is therefore useful to study simpler cases, in which gapless fermionic excitations would reside near surfaces in reciprocal space with co-dimensions larger than unity. Aside from providing a fundamentally new universality class (UC) outside of the usual bosonic ϕ^4 paradigm, theories with gapless fermions close to, for example, Dirac or parabolic points also describe physical systems of great current interest, such as graphene [4], d-wave superconductors [5], or three-dimensional gapless semiconductors [6, 7] such as gray tin, for instance. Their detailed understanding could be the stepping stone towards a more comprehensive picture of quantum phase transitions in which fermions play a decisive role in the critical behavior.

The aim of this paper is to investigate in detail fermionic criticality in lattice models where the kinetic energy provides a regularization of the Dirac Hamiltonian. In particular, we consider the Hubbard model on the honeycomb [8–13] and the π-flux lattice [14, 15]. In the absence of interactions, both lattice models have the same continuum limit given by four-component Dirac fermions per spin projection. At half-filling, the density of states is proportional to the excitation energy, and the semimetal is therefore stable against weak interactions. At strong coupling, both models map onto a Heisenberg Hamiltonian on a nonfrustrated lattice so that we expect an antiferromagnetic insulating state. The transition from the semimetal to the antiferromagnetic Mott insulator has attracted considerable interest. Starting from the weak-coupling Dirac Hamiltonian, it is natural to understand the mass generation as the signature of broken sublattice symmetry triggered by the antiferromagnetic order [12, 13]. In this case, the critical behavior is naturally described in terms of

Gross-Neveu-Yukawa theory where the broken symmetry is at the origin of mass generation [16]. In fact, at the mean-field level, mass generation can occur only as a result of symmetry breaking [17]. Starting from strong coupling, and since the transition occurs at intermediate values of the Hubbard interaction, one can follow the idea that dynamically generated higher-order ring-exchange spin processes are able to frustrate the magnetic order without closing the charge gap [18]. This scenario implies an intermediate, rotationally invariant, spin-disordered, insulating phase as proposed in Refs. [10, 11, 14].

Here, we show that a consistent and unbiased understanding of the transition is obtained by assuming a direct transition from the semimetal to the Mott insulating phase, as described by Gross-Neveu-Yukawa theory with $N_f = 2$ massless four-component Dirac fermions. In the present case, the corresponding critical behavior belongs to the so-called Gross-Neveu-Heisenberg UC, where the term Heisenberg emphasizes the SU(2) symmetry group of the order-parameter field. Within Gross-Neveu-Yukawa theory, a different number of flavors N_f as well as other symmetry groups are possible [16]. In this context, the case of $N_f = 1$ with Ising $\mathbb{Z}_2$ symmetry has been recently investigated in Refs. [19, 20] in terms of spinless fermions on the honeycomb lattice, while the case $N_f = 2$ with SU(2) symmetry has been studied in Ref. [21] by directly simulating the field theory on a lattice. Here and in the following, we restrict ourselves to the case of $N_f = 2$, which is relevant for the physics of graphene. From the perspective of Gross-Neveu-Yukawa theory with the Heisenberg SU(2) symmetry, both the honeycomb and the π-flux Hubbard lattice models are different regularizations of the same continuum theory. Hence, both models should have the same critical exponents. Our analysis of the transition is based on the notion of improved renormalization-group- (RG-) invariant quantities, defined as the ratios of magnetic correlation lengths over the lattice size. The correlation length is in fact not uniquely defined on a finite lattice. This ambiguity allows for optimization so as to reduce corrections to scaling. Using this strategy, we can unbiasedly find the value of the

critical coupling U_c and obtain critical exponents. The exponents we find for both models are consistent with the one-loop ε-expansion [16]. Most notably, the anomalous bosonic dimension η is large. Our results are based on auxiliary-field quantum Monte Carlo (QMC) simulations on lattices with up to 18×18 unit cells. Since these lattices sizes are *small*, we verify our approach for the Mott transition of the Kane-Mele-Hubbard model [22], which is known to be in the UC of the three-dimensional (3D) XY model [23–25].

The organization of the paper is the following. In Sec. II, we define the models. In Sec. III, we discuss the finite-size scaling, and in Sec. IV we provide some details about the QMC method. Section V contains our results, and Sec. VI provides a summary and the conclusions. Appendix A gives details about the definition of a correlation length in finite systems. Appendix B contains an additional finite-size scaling analysis of the Hubbard model on the honeycomb lattice which corroborates the main findings.

II. MODELS

In this work, we study three different models with a Hubbard repulsion, namely, the Hubbard model on the honeycomb lattice (*honeycomb Hubbard model*), the Hubbard model on the π-flux lattice (π-*flux Hubbard model*), and the Hubbard model on the honeycomb lattice with spin-orbit coupling (*Kane-Mele-Hubbard model*). These models are subsumed by the Hamiltonian

$$
\begin{aligned}
\mathcal{H} = \sum_{\vec{\imath},\vec{\jmath},\sigma} \hat{c}_{\vec{\imath},\sigma}^\dagger T_{\vec{\imath},\vec{\jmath}} \hat{c}_{\vec{\jmath},\sigma} &+ \mathrm{i}\,\lambda \sum_{\langle\langle \vec{\imath},\vec{\jmath}\rangle\rangle} \hat{c}_{\vec{\imath}}^\dagger \left(\vec{\nu}_{\vec{\imath},\vec{\jmath}} \cdot \vec{\sigma}\right) \hat{c}_{\vec{\jmath}} \\
&+ U \sum_{\vec{\imath}} \left(n_{\vec{\imath},\uparrow} - \frac{1}{2}\right)\left(n_{\vec{\imath},\downarrow} - \frac{1}{2}\right),
\end{aligned}
\tag{1}
$$

where $\hat{c}_{\vec{\imath},\sigma}^\dagger$ is the creation operator for an electron with spin σ at site $\vec{\imath}$ and $n_{\vec{\imath},\sigma} \equiv \hat{c}_{\vec{\imath},\sigma}^\dagger \hat{c}_{\vec{\imath},\sigma}$ is the corresponding number operator. The first term in Eq. (1) corresponds to single-particle hopping between nearest neighbors with amplitude $-t$, and across hexagons with amplitude $-t'$ (see Fig. 1). The second term couples next-to-nearest-neighbor sites and represents the intrinsic spin-orbit interaction of amplitude λ. For

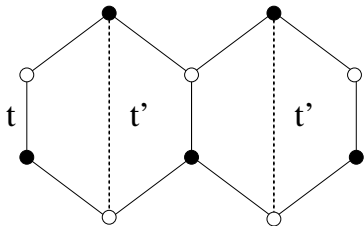
FIG. 1. Illustration of the hopping term in Eq. (1). Solid lines represent a nearest-neighbor hopping with amplitude $-t$, while dashed lines represent hopping across the hexagon with amplitude $-t'$. In this work we consider the cases $t' = 0$ (honeycomb lattice) and $t' = -t$ (π-flux lattice).

a hopping process between sites $\vec{\imath}$ and $\vec{\jmath}$ via site $\vec{r}$, $\vec{\nu}_{\vec{\imath},\vec{\jmath}} = (\vec{r} - \vec{\imath}) \times (\vec{\jmath} - \vec{r})/|(\vec{r} - \vec{\imath}) \times (\vec{\jmath} - \vec{r})| = \pm\vec{e}_z$. The spin-orbit term opens a mass gap and leads to a topological band structure [26]. If the z component of spin is conserved, the Kane-Mele model corresponds to two copies of the Haldane model [27] with opposite Chern numbers for the up and down spin sectors. The parameter $U > 0$ characterizes the Hubbard on-site repulsion. We consider the model at zero chemical potential, corresponding to half-filling.

If $\lambda = 0$ and $t' = 0$, Eq. (1) becomes the Hamiltonian of the honeycomb Hubbard model. For $\lambda = 0$ and $t' = -t$, it corresponds to the π-flux Hubbard model. The π-flux lattice emerges in the large-N limit of the Heisenberg-Hubbard model [28, 29]. Finally, for $\lambda > 0$ and $t' = 0$, Eq. (1) corresponds to the Kane-Mele-Hubbard model.

The honeycomb and π-flux Hubbard models both have a semimetallic ground state in the noninteracting case. In contrast, the spin-orbit term of the Kane-Mele-Hubbard model opens a topological band gap even for $U = 0$.

A. Honeycomb and π-flux Hubbard models ($\lambda = 0$)

For $\lambda = 0$ and $t'/t = 0, -1$, the first term in Eq. (1) gives rise to a band structure of massless Dirac fermions. At $t' = 0$, the two inequivalent cones are located at the Brillouin zone boundaries. As a function of t'/t, the cones meander (since the C_3 symmetry is broken), and are located at

$$
\vec{K} = \pm 4 \arccos\left(-\frac{(1 + t'/t)}{2}\right)(\vec{b}_1 + \vec{b}_2/2),
\tag{2}
$$

where $\vec{b}_1 = (1, -1/\sqrt{3})$ and $\vec{b}_2 = (0, 2/\sqrt{3})$. For the values of t' considered here, the cones are pinned to specific $\vec{K}$ points due to lattice symmetries. For $t' = 0$, we have the C_3 symmetry of the honeycomb lattice, whereas for $t'/t = -1$ we have the C_4 symmetry of the π-flux lattice. Expanding around $\vec{K}$ gives the spectrum

$$
E(\vec{K} + \vec{k}) = \pm\sqrt{(v_x k_x)^2 + (v_y k_y)^2} + O(k)^2, \quad \vec{k} \to 0
\tag{3}
$$

with velocities

$$
v_x = t\sqrt{1 - \frac{(1 + t'/t)^2}{4}}, \quad v_y = t\frac{\sqrt{3}\,|1 - t'/t|}{2}.
\tag{4}
$$

At $T = 0$, both the honeycomb and the π-flux Hubbard models are believed to describe a continuous phase transition between a semimetallic phase that is adiabatically connected to $U = 0$, and an insulating antiferromagnetic phase at large values of U. This phase transition has prompted numerous studies, in particular concerning the possible presence of an intermediate spin-liquid phase [10, 11]. In line with subsequent studies [12, 13], we show in the following that the phase transition is described by the Gross-Neveu-Heisenberg UC [4, 16, 31]. In this scenario, the two phases are separated by a single critical point without any intermediate phase. For the honeycomb Hubbard model, the phase diagram from
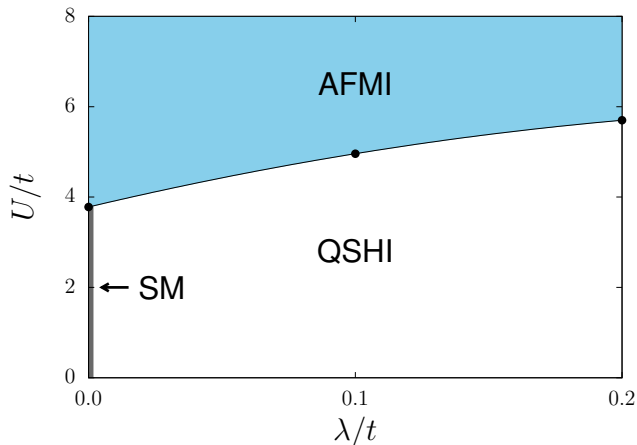
FIG. 2. (Color online) Phase diagram of the Kane-Mele-Hubbard model ($\lambda > 0$) and the honeycomb Hubbard model ($\lambda = 0$) from QMC simulations, taken from Ref. [30]. The phases correspond to a semimetal (SM), an antiferromagnetic Mott insulator (AFMI), and a quantum spin-Hall insulator (QSHI).

QMC simulations is shown in Fig. 2, where it corresponds to the $\lambda = 0$ axis.

The phase transition is characterized by the $O(3)$ antiferromagnetic order parameter

$$\vec{\phi}(\vec{x}) = \vec{S}(\vec{x}_A) - \vec{S}(\vec{x}_B), \qquad (5)$$

where $\vec{x}$ is a site of a triangular lattice that corresponds to an elementary unit cell of the honeycomb lattice, and $\vec{x}_A$ and $\vec{x}_B$ are lattice sites (in the same unit cell) that belong to the A and B sublattices, respectively.

B. Kane-Mele-Hubbard model ($\lambda \neq 0$)

In Fig. 2, we show the phase diagram of the Kane-Mele-Hubbard model from QMC simulations [30]. The model exhibits three phases, separated by second-order transition lines. For $\lambda = 0$, the model reduces to the honeycomb Hubbard model, see above. A nonzero λ opens a gap at the Dirac points, and leads to the formation of a quantum spin Hall insulator [26, 32]. At large U, the model describes an antiferromagnetic Mott insulator with magnetic order in the transverse spin direction [22–24, 33]. The Kane-Mele-Hubbard model has been studied in great detail to understand correlation effects in topological insulators [34].

The spin-orbit interaction reduces the symmetry of the Kane-Mele-Hubbard model to the $O(2)$ group. Consequently, the quantum phase transition between the quantum spin Hall phase and the antiferromagnetic Mott insulator belongs to the well known 3D XY UC [24, 25]. It is characterized by the $O(2)$ antiferromagnetic order parameter

$$\vec{\phi}(\vec{x}) = (S^x(\vec{x}_A), S^y(\vec{x}_A)) - (S^x(\vec{x}_B), S^y(\vec{x}_B)). \qquad (6)$$

In the following, we set $t = 1$.

III. FINITE-SIZE SCALING

Finite-size-scaling (FSS) theory is a powerful method that allows one to study the critical behavior of models using finite-size data. Unlike infinite-volume methods, FSS is concerned with analyzing the scaling behavior in a regime where the correlation length ξ and the linear size of the system L are of comparable size, $\xi \sim L$ [35–38]. To be precise, FSS theory allows one to formulate the scaling behavior of the observables in the so-called FSS limit, where $L, \xi \to \infty$, at fixed ξ/L. The FSS method has been recently discussed in the context of quantum phase transitions in Ref. [39].

We consider the spatial two-point correlation function $C(\vec{x} - \vec{y})$ of the order parameter $\phi(\vec{x})$ at $T = 0$,

$$C(\vec{x} - \vec{y}) \equiv \langle \vec{\phi}(\vec{x}) \cdot \vec{\phi}(\vec{y}) \rangle. \qquad (7)$$

Using the spatial correlations $C(\vec{x})$ one can define various observables, the FSS behavior of which allows one to study the critical properties of second-order phase transitions. We study the zero-momentum Fourier transform of the two-point function χ, defined as

$$\chi(U, L) \equiv \sum_{\vec{x}} C(\vec{x}). \qquad (8)$$

Close to a second-order phase transition at $U = U_c$, χ exhibits the following FSS behavior [39]

$$\chi(U, L) = L^{2-z-\eta} \left[f_\chi(w) + L^{-\omega} g_\chi(w) \right] + B(U), \quad (9)$$

$$w \equiv u L^{1/\nu}, \qquad u \equiv (U - U_c)/U_c, \qquad (10)$$

where ν, η, and z are universal critical exponents, ω is a generic correction-to-scaling exponent and $B(U)$ is a nonuniversal analytic background term that originates from the nonuniversal, short-distance behavior of $C(x)$, i.e., from the terms in the sum of Eq. (8) for which $|\vec{x}| \ll L$. According to RG theory, corrections to scaling may have several origins (see also Ref. [39]):

(i) Irrelevant operators give rise to scaling corrections with an exponent ω equal to their negative RG dimension.

(ii) Analytical scaling corrections originate from the so-called nonlinear scaling fields [40], according to which the scaling fields are replaced by a generic analytical expansion in the Hamiltonian parameters. For instance, u in Eq. (10) should be replaced by an expansion of the form $u + cu^2 + o(u^2)$, where c is a nonuniversal constant, resulting in a scaling correction with exponent $\omega = 1/\nu$.

(iii) Additional scaling corrections arise from the analytic part of the free energy. This is the case of the background term $B(U)$, which can be considered as a subleading term with an effective correction-to-scaling exponent $\omega = 2 - z - \eta$.

In general, one expects several correction-to-scaling terms, the leading one being the one with the smallest exponent ω. Here and in the following, we consider the leading scaling correction only.

RG-invariant quantities (also called phenomenological couplings) are instrumental for investigating the critical behavior.

Here, we consider ratios of the correlation length and the lattice size L. As explained in Appendix A, on a finite lattice there is no unique definition of the correlation length. We defined several correlation lengths that mimic the definition of the second-moment correlation length of the two-point function $C(\vec{x})$; all these quantitites are observables that scale as $\propto L$ in the FSS limit, so that their ratio with the lattice size L is RG-invariant. We consider

$$R_\xi^{(1)}(U, L) \equiv \xi^{(1)}(U, L)/L, \qquad (11)$$

$$R_\xi^{(2)}(U, L) \equiv \xi^{(2)}(U, L)/L, \qquad (12)$$

$$R_\xi(U, L) \equiv \xi(U, L)/L, \qquad (13)$$

$$R_{\xi,s,\kappa,\rho}(U, L) \equiv \xi_{s,\kappa,\rho}(U, L)/L, \qquad (14)$$

where $\xi^{(1)}$, $\xi^{(2)}$ are two finite-size correlation lengths defined in terms of the Fourier transform of $C(\vec{x})$ and corresponding to the two principal directions, ξ is a generalized f-mean value of $\xi^{(1)}(L)$ and $\xi^{(2)}(L)$, and $\xi_{s,\kappa,\rho}$ is a correlation length defined in terms of the two-point function $C(\vec{x})$ in real space. These correlation lengths are inequivalent observables in the FSS limit; their definitions are discussed in Appendix A. The parameters κ and ρ that enter in the definition of $\xi_{s,\kappa,\rho}$ are scale-invariant ratios that influence the amplitude of the scaling corrections (see Appendix A 3).

As discussed in Sec. IV, our simulation data for the π-flux Hubbard model are for lattices with $L_1 = L/2$ unit cells in direction 1 and $L_2 = L$ unit cells in direction 2. In view of the anisotropy of the lattice, we use a slightly different definition for the RG-invariant quantity $R_\xi^{(1)}$:

$$R_\xi^{(1)}(U, L) \equiv \xi^{(1)}(U, L)/(L/2) \quad (\pi\text{-flux lattice}). \qquad (15)$$

According to FSS theory, a generic RG-invariant observable $R(U, L)$ obeys the scaling ansatz

$$R(U, L) = f_R(w) + L^{-\omega}g_R(w), \qquad (16)$$

where the function $f_R(w)$ is universal, apart from a nonuniversal normalization of the scaling variable w. Aside from depending on the UC of the phase transition, $f_R(w)$ also depends on the boundary conditions of the system and on the aspect ratio. In Eq. (16), we have included a correction-to-scaling term $L^{-\omega}g_R(w)$, which decays with a correction-to-scaling exponent ω.

As illustrated in Appendix A, the finite-size correlation lengths $\xi^{(1)}$, $\xi^{(2)}$, ξ, and $\xi_{s,\kappa,\rho}$ are computed with a ratio that involves χ [see Eq. (8)]. Therefore, scaling corrections for $R_\xi^{(1)}(U, L)$, $R_\xi^{(2)}(U, L)$, R_ξ, and $R_{\xi,s,\kappa,\rho}$ are analogous to those of χ. In particular, they are also affected by scaling corrections that decay with an exponent $\omega = 2 - z - \eta$ and originate from the analytic part of the free energy.

A popular method for extracting the critical coupling U_c from the FSS behavior of a model is the so-called crossing method. It is based on the observation that, neglecting scaling corrections in Eq. (16) (i.e., taking $\omega \to \infty$), the equation

$$R(U, L) = R(U, L') \qquad (17)$$

admits a solution for $U = U_c$, i.e., $u = 0$. If in an interval around $u = 0$ the scaling function $f_R(w)$ is monotonic, then, locally, this is the only solution to Eq. (17). This implies that the curves $R(U, L)$ as a function of U intersect at $U = U_c$ for all lattice sizes L. Typically, one observes instead a drift in the crossings, which is due to scaling corrections. To determine the critical coupling U_c, one usually defines a pseudocritical coupling $U_{c,R}(L)$ as the solution of Eq. (17) with $L' = \alpha L$, where α is a fixed ratio. Here, the available lattice sizes do not allow us to use this definition for $U_{c,R}(L)$. Instead, we define a pseudocritical coupling $U_{c,R}(L)$ as the solution of Eq. (17) with $L' = L + c$, that is,

$$R(U_{c,R}(L), L) = R(U_{c,R}(L), L + c), \qquad (18)$$

where c is a fixed constant. By inserting Eq. (16) in Eq. (18), and expanding for $L \to \infty$, one can show that for $L \to \infty$ $U_{c,R}(L) \to U_c$ according to

$$U_{c,R}(L) = U_c + AL^{-e}, \qquad e = 1/\nu + \omega, \qquad (19)$$

where A is a nonuniversal constant. Using different RG-invariant quantities, we can define different pseudocritical couplings $U_{c,R}(L)$ that all converge to U_c for $L \to \infty$. This property can be used to corroborate the result for U_c.

IV. QUANTUM MONTE CARLO METHOD

We used the projective auxiliary-field QMC algorithm to compute the spin-spin correlations. Because a detailed discussion of the algorithm is beyond the scope of this work, we refer the reader to Refs. [24, 41].

Ground-state expectation values of observables are calculated according to the equation

$$\langle \hat{O} \rangle_0 = \lim_{\Theta \to \infty} \frac{\langle \Psi_T | e^{-\Theta \hat{H}} \hat{O} e^{-\Theta \hat{H}} | \Psi_T \rangle}{\langle \Psi_T | e^{-2\Theta \hat{H}} | \Psi_T \rangle}, \qquad (20)$$

where the ground-state wave function is filtered out of a trial wave function (required to be nonorthogonal to the ground state) by projection along the imaginary-time axis. The QMC algorithm relies on a Trotter decomposition. We used a symmetric version that produces a systematic error of the order $(\Delta\tau)^2$, where $\Delta\tau$ is the imaginary-time step. We typically used $\Delta\tau = 0.1$, and a projection parameter $\Theta = 30$. The trial wave function was taken to be the ground state of the noninteracting Hamiltonian and chosen to be a spin singlet. The method has two sources of systematic errors: the projection parameter and the high-energy (or short imaginary-time) cutoff $\Delta\tau$. For a given statistical precision of 0.1% for the antiferromagnetic order parameter, we checked that the choice of the projection parameter and trial wave function guarantees convergence to the ground state. On the other hand, at $U_c = 3.8$ and for the honeycomb lattice, the finite value of $\Delta\tau$ leads to a systematic error of the order of 0.5%. This high-energy cutoff may slightly shift the critical values of U at which the transition occurs but should not alter the
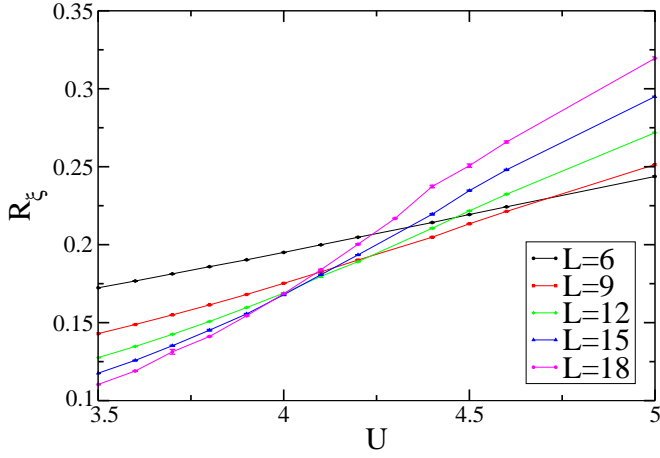
FIG. 3. (Color online) RG-invariant quantity R_ξ for the honeycomb Hubbard model. Lines are guides to the eye.

universality. Finally, we used an SU(2)-symmetric Hubbard-Stratonovich transformation [41] to ensure that this symmetry is conserved for each field configuration.

For the simulations on the honeycomb lattice we used lattices spanned by the vectors $\vec{L}_1 = L\vec{a}_1$ and $\vec{L}_2 = L\vec{a}_2$, where $\vec{a}_1 = (1, 0)$ and $\vec{a}_2 = (1/2, \sqrt{3}/2)$, and with boundary conditions $c_{\vec{i}+\vec{L}_n,\sigma} = c_{\vec{i},\sigma}$ with $n = 1, 2$. With this choice of boundary conditions, and the values of L as multiples of 3, the Dirac points are part of the reciprocal lattice.

For the π-flux lattice we considered lattices defined by the vectors $\vec{L}_1 = \frac{L}{2}\vec{a}_1$ and $\vec{L}_2 = \frac{L}{2}(2\vec{a}_2 - \vec{a}_1)$, again with boundary conditions $c_{\vec{i}+\vec{L}_n,\sigma} = c_{\vec{i},\sigma}$. This choice of boundary conditions is equivalent to a lattice that extends over $L_1 = L/2$ unit cells in the $\vec{a}_1$ direction and over $L_2 = L$ unit cells in the $\vec{a}_2$ direction. The total number of two-site unit cells is $L \times L/2$, and the total number of lattice sites is $L \times L/2 \times 2 = L \times L$. This also makes the lattice equivalent to an $L \times L$ square lattice. For L being a multiple of 4 the
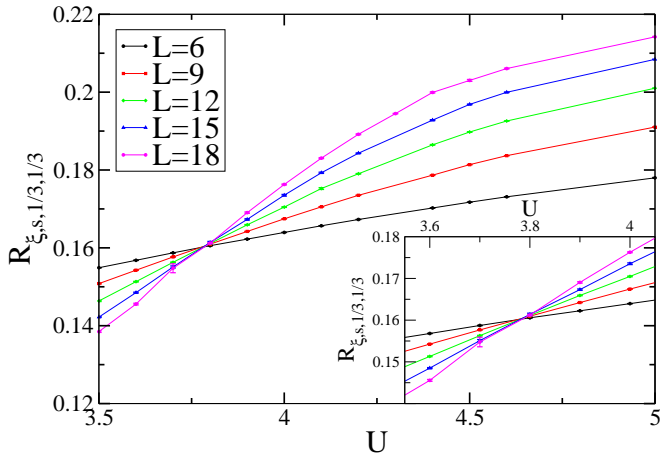

FIG. 4. (Color online) Same as Fig. 3 for $R_{\xi,s,1/3,1/3}$. Inset: magnification of the data close to their crossing at $U \approx 3.8$.
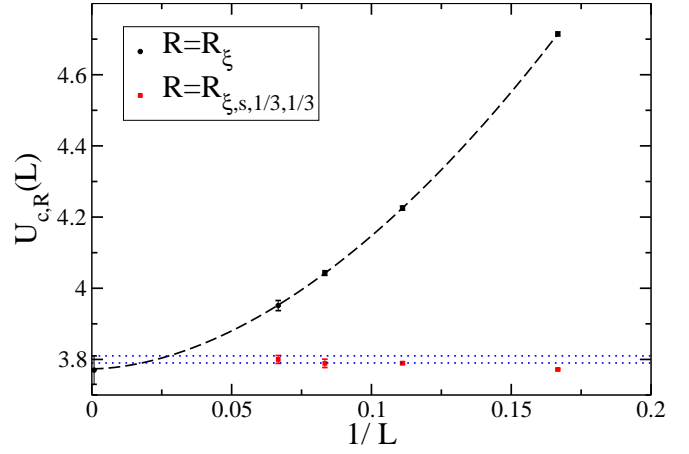

FIG. 5. (Color online) pseudocritical coupling $U_{c,R}$ for the honeycomb Hubbard model, obtained by numerically solving Eq. (18) for two phenomenological couplings $R = R_\xi$ and $R = R_{\xi,s,1/3,1/3}$. The plotted value of $U_{c,R_\xi} = 3.77(4)$ for $L \to \infty$ has been obtained by fitting the data to Eq. (19). The dashed line represents the right-hand side of Eq. (19), with central values of the fit $U_c = 3.77$, and $e = 1.8$. The dotted lines indicate the interval in the final estimate of the critical coupling $U = 3.80(1)$ as reported in Eq. (27).

Dirac points are part of the reciprocal lattice.

V. RESULTS

A. Honeycomb Hubbard model

We simulated the honeycomb Hubbard model on lattices with $L = 6, 9, 12, 15,$ and 18. As discussed in Appendix A 3, the correlation length $\xi_{s,\kappa,\rho}$ is computed for $\kappa = \rho = 1/3$ only. In Figs. 3 and 4 we show the RG-invariant quantities $R_\xi(U, L)$ and $R_{\xi,s,1/3,1/3}(U, L)$ as a function of U and for lattice sizes $L = 6 - 18$. We observe that the curves of $R_\xi(U, L)$ for different L do not show a common intersection point, but exhibit a systematic drift of the intersection points from $U \approx 4.7$ (the crossing point of the curves for $L = 6$ and $L = 9$) towards smaller values of U; the data for $R_\xi(U, L)$ and for the two largest lattice sizes intersect at $U \approx 3.9 - 4$. The curves of $R_{\xi,s,1/3,1/3}(U, L)$ shown in Fig. 4 exhibit instead a common intersection at $U \approx 3.8$.

These observations are confirmed by the analysis of the pseudocritical coupling $U_{c,R}(L)$. In Fig. 5, we show $U_{c,R}(L)$ as a function of $1/L$, as obtained by numerically solving Eq. (18), with $R = R_\xi$, $R_{\xi,s,1/3,1/3}$ and $c = 3$. For each pair of lattice sizes L and $L + 3$ we fitted the data for R_ξ and $R_{\xi,s,1/3,1/3}$ to a suitable Taylor expansion in U in an interval around the crossing point. These fits provide an interpolation of the curves for $R(U, L)$ and $R(U, L + 3)$ that, in turn, allows us to solve Eq. (18). The resulting error bar of $U_R(L)$, which is determined from the covariance matrix of the coefficients of the fits used to interpolate $R(U, L)$, may underestimate the uncertainty in $U_R(L)$ because it does not take into account a possible systematic error in the trunca-

tion of the Taylor expansion of $R(U, L)$. Figure 5 reveals that $U_{c,R_\xi}(L)$ decreases slowly upon increasing L, whereas $U_{c,R_{\xi,s,1/3,1/3}}(L)$ remains stable; for $L \geq 9$, $U_{c,R_{\xi,s,1/3,1/3}}(L)$ is constant within error bars. In order to extrapolate U_c from the pseudocritical coupling $U_{c,R_\xi}(L)$, we fitted the data for $U_{c,R_\xi}(L)$ to the right-hand side of Eq. (19), leaving U_c, A, and the exponent e as free parameters. The fitted values are $U_c = 3.77(4)$ and $e = 1.8(1)$, with $\chi^2/\text{DOF} = 0.02$ (DOF: degrees of freedom). Within the statistical precision, the result for $U_c = 3.77(4)$ is in full agreement with the pseudocritical couplings $U_{c,R_{\xi,s,1/3,1/3}}(L)$ for all available lattice sizes. In Fig. 5, we also show the right-hand side of Eq. (19) (the dashed line), which illustrates the convergence of $U_{c,R_\xi}(L)$ to the critical coupling U_c for $L \to \infty$.

The slow convergence of $U_{c,R_\xi}(L)$ to U_c implies that R_ξ is affected by large scaling corrections. As discussed in Sec. III, these can stem from various sources. As shown in the analysis below, the critical behavior belongs to the Gross-Neveu-Heisenberg UC. Using functional RG methods, the leading irrelevant operator in this UC has been determined as $\omega \approx 0.9$ [42]. In the present model, an additional irrelevant operator is associated with the restoration of the Lorentz symmetry; within the ε-expansion, its negative dimension is $\omega = \frac{4}{5}\varepsilon$ [16], where one should set $\varepsilon = 1$ for the two-dimensional system considered here. Although such a simple substitution has to be taken with some care, we have no reason to presume the existence of an irrelevant operator with a small ω exponent. Analytical scaling corrections arising from nonlinear scaling fields are also not expected to play an important role here. Indeed, as we show in the following, $\nu \lesssim 1$, so that scaling corrections $\propto L^{-1/\nu}$ are not particularly large. On the other hand, in the Gross-Neveu picture, the dynamical exponent z is equal to 1, and field theoretical methods indicate a large η exponent. Within the first-order ε-expansion, one has $\eta = \frac{4}{5}\varepsilon$ [16], so that by setting $\varepsilon = 1$ one obtains a rather large value of the η exponent, $\eta = 0.8$. A large η exponent is also confirmed by the analysis below. Therefore, we expect the zero-momentum Fourier transform of the two-point function χ as well as the RG-invariant quantities R_ξ, $R_{\xi,s}$ to be affected by slowly-decaying scaling corrections, with $\omega = 2 - z - \eta \approx 0.2$. However, the amplitude of such scaling corrections is not universal and also depends on the specific observable. The stable crossing point observed in Fig. 4 indicates that the correction to scaling $\propto L^{-0.2}$ is in fact suppressed in $R_{\xi,s,1/3,1/3}$, i.e., $R_{\xi,s,1/3,1/3}$ is effectively an (approximately) "improved" observable [1].

In view of these results, we determined the critical exponent ν and the critical coupling U_c by exploiting the FSS behavior of $R_{\xi,s,1/3,1/3}$. Following a procedure analogous to the one employed in Ref. [44], we fitted $R_{\xi,s,1/3,1/3}$ to a Taylor expansion of Eq. (16). We restricted the analysis to the data where U belongs to an interval $[3.6, 4]$ centered at

---

[1] We notice that the construction of improved observables, as well as improved models, where leading scaling corrections are suppressed requires in general a fine-tuning of an irrelevant parameter, see, e.g., the discussion in Ref. [43].

$U = 3.8$, which is the approximate common intersection of the curves in Fig. 4. Within this interval we can expand the scaling function $f_R(w)$ for $R = R_{\xi,s,1/3,1/3}$ in powers of w. Using Eq. (10) in Eq. (16) and neglecting scaling corrections, we obtain

$$R = R^* + \sum_{n=1}^{n_{\max}} a_n (U - U_c)^n L^{n/\nu}. \tag{21}$$

We fitted the data for $R = R_{\xi,s,1/3,1/3}$ to Eq. (21), leaving the universal critical value $R^*_{\xi,s,1/3,1/3} \equiv R^*$, the coefficients $\{a_i\}$, U_c, and ν as free parameters. In order to monitor the role of the neglected scaling corrections, we repeated the fits disregarding systematically the smallest lattice sizes. Moreover, to check the reliability of the Taylor expansion in Eq. (21), we repeated the fit for $n_{\max} = 1, 2,$ and 3.

In Table I we report the fit results as a function of the minimum lattice size $L_{\min}$ taken into account, and the expansion order $n_{\max}$. Table I reveals that χ^2/DOF decreases significantly between $n_{\max} = 1$ and $n_{\max} = 2$, but only marginally between $n_{\max} = 2$ and $n_{\max} = 3$. This indicates that within the available numerical precision, the range of U considered here does not allow a linear approximation of $f_{R_{\xi,s,1/3,1/3}}(w)$, whereas a quadratic approximation appears to be adequate. Thus, we can restrict the discussion of the results to the case $n_{\max} = 2$. The corresponding fits show a good χ^2/DOF for $L_{\min} \geq 9$; only for $L_{\min} = 6$ we have a large χ^2/DOF, indicating sizable scaling corrections. Moreover, the fitted parameters appear to be rather stable upon increasing $L_{\min}$. A conservative judgment of the fit results would give the estimates $U_c = 3.793(5)$, $\nu = 0.84(4)$, and $R^*_{\xi,s,1/3,1/3} = 0.1608(2)$; these values agree with the results for $L_{\min} = 9, 12$, including a variation of one error bar, and with the central value of the less precise fit results for $L_{\min} = 15$. As a further check of the reliability of these results, we repeated the fits with a smaller interval in U where a linear approximation of $f_{R_{\xi,s,1/3,1/3}}(w)$ is reliable. In Table II we report the results of the fits of $R_{\xi,s,1/3,1/3}$ to Eq. (21) with $n_{\max} = 1$ and $U \in [3.7, 3.9]$. For $L_{\min} \geq 9$, these results display a good χ^2/DOF and are in full agreement with the estimates of U_c, ν, and $R^*_{\xi,s,1/3,1/3}$ given above. These estimates were obtained by an FSS analysis that neglects scaling corrections. As discussed in the following, the inclusion of scaling corrections results in slightly less precise estimates for U_c and $R^*_{\xi,s,1/3,1/3}$.

The exponent η can be determined by analyzing the FSS behavior of χ. To avoid using the values of U_c and ν determined above, we invert Eq. (16) to obtain the scaling variable w as a function of R. Then, Eq. (9) can be rewritten as

$$\chi(R, L) = L^{2-z-\eta} f_{\chi,R}(R), \tag{22}$$

where corrections to scaling have been neglected. Since the previous analysis has shown that $R_{\xi,s,1/3,1/3}$ is affected by small scaling corrections, we chose to analyze χ using $R = R_{\xi,s,1/3,1/3}$. In Fig. 6 we show χ as a function of $R_{\xi,s,1/3,1/3}$. The fact that χ slowly grows with L suggests a small value of the exponent $2 - z - \eta$ that appears in Eq. (22).

For a quantitative analysis of the exponent η we fitted $\chi(R, L)$ to a Taylor expansion of the right-hand side of

TABLE I. Results of the fits of $R = R_{\xi,s,1/3,1/3}$ for the honeycomb Hubbard model to Eq. (21) (first three sets) and to Eq. (26) (last three sets), with $U \in [3.6, 4]$. $L_{\min}$ is the minimum lattice size taken into account in the fits.

	$L_{\min}$	U_c	ν	$R^*_{\xi,s,1/3,1/3}$	χ^2/DOF
	6	3.782(1)	0.758(4)	0.16017(3)	443.2/21
$n_{\max} = 1$	9	3.7954(15)	0.816(7)	0.16077(6)	39.5/16
	12	3.7975(30)	0.87(2)	0.1609(2)	17.8/11
	15	3.798(9)	0.91(5)	0.1610(6)	9.5/6
	6	3.775(1)	0.747(4)	0.16004(3)	331.0/20
$n_{\max} = 2$	9	3.790(2)	0.812(7)	0.16063(7)	18.0/15
	12	3.792(3)	0.86(2)	0.1607(2)	5.0/10
	15	3.797(8)	0.87(5)	0.1610(6)	3.4/5
	6	3.780(1)	0.694(6)	0.16014(3)	240.0/19
$n_{\max} = 3$	9	3.791(2)	0.786(15)	0.16066(7)	14.7/14
	12	3.792(4)	0.85(3)	0.1607(2)	4.9/9
	15	3.797(8)	0.86(6)	0.1610(6)	3.3/4
$n_{\max} = 2$	6	3.823(4)	0.755(4)	0.175(1)	167.4/19
$m_{\max} = 0$	9	3.805(11)	0.813(7)	0.167(5)	16.0/14
$\omega = 0.15$	12	3.82(5)	0.86(2)	0.18(3)	4.6/9
$n_{\max} = 2$	6	3.820(4)	0.754(4)	0.1679(6)	166.5/19
$m_{\max} = 0$	9	3.804(10)	0.813(7)	0.164(2)	16.01/14
$\omega = 0.3$	12	3.82(4)	0.86(2)	0.168(14)	4.6/9
$n_{\max} = 2$	6	3.816(3)	0.754(4)	0.1653(4)	165.7/19
$m_{\max} = 0$	9	3.803(9)	0.813(7)	0.1629(16)	16.0/14
$\omega = 0.45$	12	3.82(4)	0.86(2)	0.166(9)	4.6/9

TABLE II. Same as Table I for $U \in [3.7, 3.9]$ and $n_{\max} = 1$.

$L_{\min}$	U_c	ν	$R^*_{\xi,s,1/3,1/3}$	χ^2/DOF
6	3.7809(15)	0.74(1)	0.16020(5)	140.0/11
9	3.792(2)	0.80(2)	0.16069(9)	8.1/8
12	3.794(5)	0.87(5)	0.1608(3)	2.6/5
15	3.80(1)	0.75(12)	0.1613(8)	1.6/2

Eq. (22), using the QMC data for which $R_{\xi,s,1/3,1/3} \in [0.151, 0.171]$; for the central lattice size $L = 12$, this interval in $R_{\xi,s,1/3,1/3}$ corresponds to the range $U \in [3.6, 4]$ that we used in the analysis of the ν exponent. We performed a fit of the data for $\chi(U, R)$ to

$$\chi(R, L) = L^{1-\eta'} \sum_{n=0}^{n_{\max}} a_n R^n, \quad \eta' \equiv \eta + z - 1, \quad (23)$$

with $R = R_{\xi,s,1/3,1/3}$ and leaving η' and $\{a_n\}$ as free parameters. In Eq. (23) we have introduced for convenience the exponent η', which is defined such that $\eta' = \eta$ if $z = 1$. In Table III, we report the fit results as a function of $n_{\max}$ and the minimum lattice size $L_{\min}$ taken into account. We observe that χ^2/DOF substantially decreases upon increasing the expansion order from $n_{\max} = 1$ to $n_{\max} = 2$, while no appreciable difference is found upon further increasing $n_{\max}$ to $n_{\max} = 3$. Clearly, a parabolic approximation $n_{\max} = 2$ is sufficient to describe our MC data in the interval
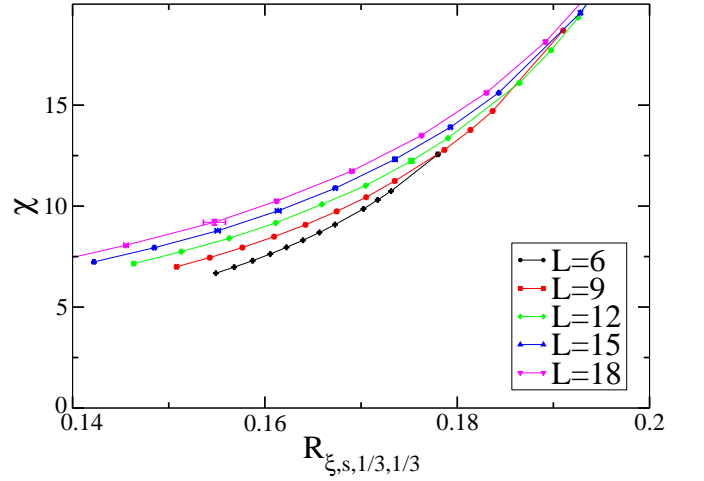

FIG. 6. (Color online) The two-point function at zero momentum χ as a function of the RG-invariant observable $R_{\xi,s,1/3,1/3}$. Lines are guides to the eye.

$R_{\xi,s,1/3,1/3} \in [0.151, 0.171]$. On the other hand, the χ^2/DOF is large and acquires a small value for $L_{\min} = 12$ only. This shows that scaling corrections give an important contribution. Indeed, the fits indicate a value $\eta' \approx 0.7$: for such a value of η' the background contribution to χ results in corrections to

TABLE III. Results of the fit of χ for the honeycomb Hubbard model to Eq. (23) (first three sets) and to Eq. (24) (last set), with $R = R_{\xi,s,1/3,1/3}$ and $R_{\xi,s,1/3,1/3} \in [0.151, 0.171]$. The critical exponent η' is defined as $\eta' \equiv \eta + z - 1$, such that $\eta' = \eta$ if $z = 1$. $L_{\min}$ is the minimum lattice size taken into account.

	$L_{\min}$	η'	χ^2/DOF
	6	0.771(2)	1759.7/23
$n_{\max} = 1$	9	0.746(4)	445.0/14
	12	0.759(9)	65.4/8
	6	0.766(2)	1264.3/22
$n_{\max} = 2$	9	0.746(4)	66.8/13
	12	0.746(9)	6.8/7
	6	0.765(2)	1241.7/21
$n_{\max} = 3$	9	0.746(4)	66.6/12
	12	0.746(9)	6.8/6
$n_{\max} = 2$	6	0.57(4)	112.7/20
$m_{\max} = 1$	9	0.70(15)	6.2/11

scaling with a rather small exponent $\omega = 1 - \eta' \approx 0.3$.

We thus consider the presence of an analytical background and fit our data to

$$\chi(R, L) = L^{1-\eta'} \sum_{n=0}^{n_{\max}} a_n R^n + \sum_{m=0}^{m_{\max}} b_m R^m, \quad \eta' \equiv \eta + z - 1,$$
(24)

with $R = R_{\xi,s,1/3,1/3}$. In Table III, we also report the fit results with $n_{\max} = 2$ and $m_{\max} = 1$ for different $L_{\min}$. While the fit done using all the available lattices shows a large χ^2/DOF, indicating the presence of additional scaling corrections beyond those taken into account in Eq. (24), a good χ^2/DOF is found for $L_{\min} = 9$. The fitted value of η' is in full agreement with the results of the fits to Eq. (23) given in Table III (above); its error bar, which is significantly larger than the one of the values obtained by the fits to Eq. (23) gives a measure of the influence of the slowly-decaying scaling corrections due to the background contribution that is neglected in the fits to Eq. (23). Moreover, the fitted value of η' for $L_{\min} = 9$ agrees with the corresponding result for $L_{\min} = 6$. Accordingly, we can regard the fit results for $L_{\min} = 9$ with its uncertainty as a safe determination of the η' exponent. We thus quote as a final result:

$$\begin{aligned} \eta' = \eta + z - 1 &= 0.70(15), \\ \eta &= 0.70(15) \quad (\text{if } z = 1). \end{aligned}$$
(25)

The estimate of Eq. (25) implies that the analytical part of the free energy gives rise to slowly-decaying scaling corrections with an effective correction-to-scaling exponent $\omega = 2 - z - \eta = 0.30(15)$. In view of the relatively small available lattice sizes, we repeated the FSS analysis of $R_{\xi,s,1/3,1/3}$, this time including scaling corrections, with the aim of checking the reliability of the estimates for U_c, ν, and $R_{\xi,s,1/3,1/3}^*$ obtained above by neglecting scaling corrections. Indeed, even if the RG-invariant observable $R_{\xi,s,1/3,1/3}$ appears to show small scaling corrections, such a small value of ω may give

rise to a drift in the estimates of the critical parameters that is larger than the statistical error bar. We fitted $R_{\xi,s,1/3,1/3}$ to a Taylor expansion of Eq. (16):

$$R = R^* + \sum_{n=1}^{n_{\max}} a_n (U - U_c)^n L^{n/\nu}$$
$$+ L^{-\omega} \sum_{m=0}^{m_{\max}} b_m (U - U_c)^m L^{m/\nu}.$$
(26)

In Table I, we also report the fit results obtained for fixed $\omega = 0.15, 0.3, 0.45$, which reveal that the fitted value of ν is stable and in perfect agreement with the estimate obtained by neglecting scaling corrections. However, we observe that U_c and $R_{\xi,s,1/3,1/3}^*$ exhibit a deviation with respect to the previously obtained values $U_c = 3.793(5)$, $R_{\xi,s,1/3,1/3}^* = 0.1608(2)$. The variation in U_c is rather small, but larger than the error bars, whereas the critical-point value $R_{\xi,s,1/3,1/3}^*$ exhibits a larger variation. Indeed, residual scaling corrections affect in a statistically significant way the fitted values of U_c and $R_{\xi,s,1/3,1/3}^*$. Therefore, we choose more conservative error bars for U_c and $R_{\xi,s,1/3,1/3}^*$, which take into account the results of Table I, with and without considering corrections to scaling. We obtain the estimates

$$U_c = 3.80(1),$$
(27)

$$\nu = 0.84(4),$$
(28)

$$R_{\xi,s,1/3,1/3}^* = 0.166(5).$$
(29)

The final estimate for U_c is also in full agreement with the less precise estimate obtained by extrapolating the pseudocritical coupling $U_{c,R_\xi}(L)$ (see Fig. 5).

As a further check of the results presented in this section, we performed an additional FSS analysis of χ as a function of U and L, as done for the RG-invariant quantity $R_{\xi,s,1/3,1/3}$. The corresponding results are presented in Appendix B and corroborate the reliability of the obtained estimates.

B. Kane-Mele-Hubbard model

We simulated the Kane-Mele-Hubbard model for lattice sizes $L = 6, 9, 12, 15$, and 18, setting the spin-orbit coupling $\lambda = 0.2$. In Fig. 7 (Fig. 8) we show the RG-invariant quantity $R_\xi(U, L)$ [$R_{\xi,s,1/3,1/3}(U, L)$] as a function of U and for different lattice sizes L. We observe that the curves of $R_\xi(U, L)$ for $L \geq 9$ show a common intersection point at $U \approx 5.71$, whereas the data for $R_{\xi,s,1/3,1/3}(U, L)$ exhibit a systematic drift of the intersection point from $U \approx 5.5$ (the crossing point of the curves for $L = 6$ and $L = 9$) towards larger values of U. In Fig. 9, we show the pseudocritical couplings $U_{c,R}(L)$ as a function of the inverse lattice size L, computed with the method mentioned in Sec. V A. Consistent with Figs. 7 and 8, $U_{c,R_\xi}(L)$ is constant within error bars for $L \geq 9$, while $U_{c,R_{\xi,s,1/3,1/3}}(L)$ increases with L. A fit of the
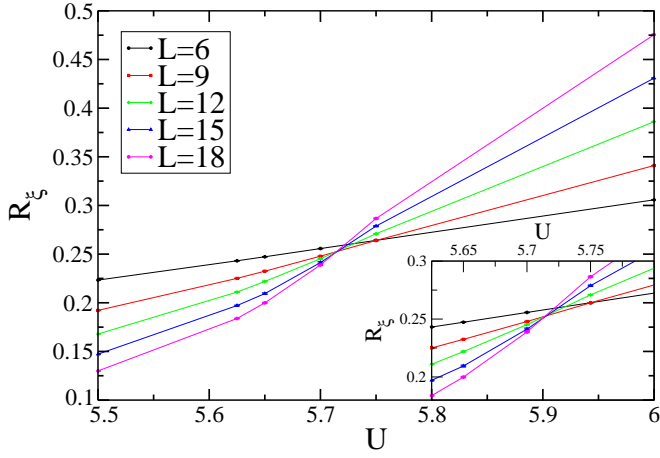
FIG. 7. (Color online) RG-invariant quantity R_ξ for the Kane-Mele-Hubbard model. Lines are guides to the eye. Inset: magnification of the data close to their crossing at $U \approx 5.7$.
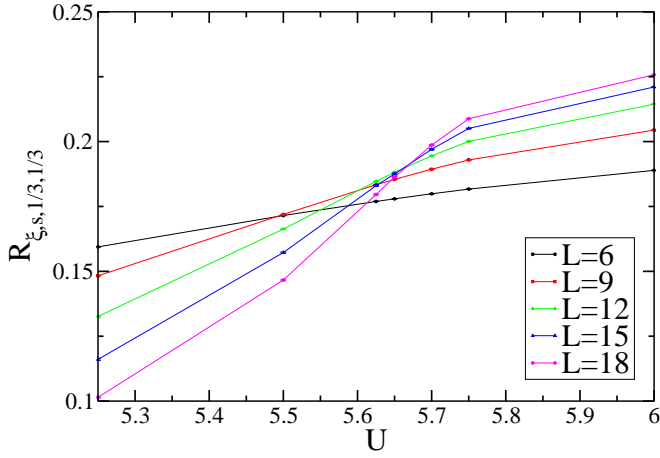

FIG. 9. (Color online) Same as Fig. 5 for the Kane-Mele-Hubbard model. The plotted value of $U_{c,R_{\xi,s,1/3,1/3}} = 5.73(1)$ for $L \to \infty$ has been obtained by fitting the data to Eq. (19). The dashed line represents the right-hand side of Eq. (19), with central values of the fit $U_c = 5.73$. The dotted lines indicate the interval in the final estimate of the critical coupling $U = 5.71(1)$ as reported in Eq. (30).

FIG. 8. (Color online) Same as Fig. 7 for $R_{\xi,s,1/3,1/3}$.

results for $U_{c,R_{\xi,s,1/3,1/3}}(L)$ to Eq. (19) gives $U_c = 5.73(1)$, with a large $\chi^2/\mathrm{DOF} = 22.5$. This suggests the presence of competing scaling corrections in $R_{\xi,s,1/3,1/3}(U,L)$, which are not captured by Eq. (19). For this reason, the precision on the resulting value of $U_c = 5.73(1)$ has to be taken with caution, as it can be affected by a systematic error. The limited lattice sizes available do not allow us to further investigate the reliability of this result. Our final estimate of U_c is based on the FSS analysis of R_ξ (see following). In Fig. 9, we also show the right-hand side of Eq. (19), as fitted using the data for $U_{c,R}(L)$ with $R = R_{\xi,s,1/3,1/3}$. In line with the considerations on the presence of a superposition of corrections to scaling, some data points show a significant deviation from the fitted curve.

In order to determine the critical exponent ν and the critical coupling U_c, we analyzed the FSS behavior of R_ξ which, in this case, appears to have reduced scaling corrections. We restrict the analysis to the interval $U \in [5.625, 5.75]$, around
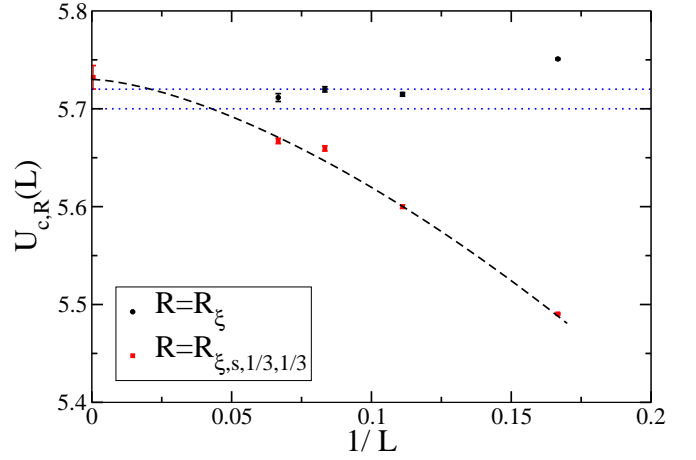
the expected critical point $U_c \approx 5.7$, as inferred from the analysis of the pseudocritical couplings. In Table IV, we report the results of the fits of R_ξ to Eq. (21). We observe that χ^2/DOF decreases significantly when we increase $n_{\max}$ from $n_{\max} = 1$ to $n_{\max} = 2$, and only marginally when $n_{\max}$ is set to $n_{\max} = 3$. Thus, a quadratic approximation should be adequate to describe the data for R_ξ in the interval $U \in [5.625, 5.75]$. The fits with $n_{\max} = 2$ show large values of χ^2/DOF for $L_{\min} = 6$, indicating important scaling corrections, and still a somewhat large value of χ^2/DOF for $L_{\min} = 9$, suggesting the presence of residual scaling corrections for $L = 9$. The χ^2/DOF ratio is good for $L_{\min} \geq 12$. The fitted values of U_c, ν, and R_ξ^* are essentially stable for $L_{\min} \geq 9$. Upon conservatively judging the variation of the fit results for ν as obtained by these fits, one can extract an estimate $\nu = 0.68(3)$. This value agrees with that of the 3D XY UC, $\nu = 0.6717(1)$ [45] (see the discussion in Sec. II). In view of value of χ^2/DOF for $L_{\min} = 9$, we repeated the analysis by including scaling corrections. Our data do not allow an independent determination of the ω exponent. Nevertheless, since we expect that the critical behavior belongs to the 3D XY UC and since our fits to Eq. (21) are consistent with this picture, we fitted R_ξ to Eq. (26), fixing ω to the value of the leading irrelevant operator for the 3D XY UC, $\omega = 0.785(20)$ [45]. The corresponding fit results are given in Table IV where, for completeness, we also report the results of fits to Eq. (26) with $n_{\max} = 3$. The results of the fits do not change significantly upon varying $\omega = 0.785(20)$ within one error bar. For this reason, we report the fit results obtained by fixing ω to its central value $\omega = 0.785$.

The inclusion of a correction-to-scaling term in the fits results in a large reduction of the χ^2/DOF ratio for the fits with $L_{\min} = 6$, whose corresponding results align to those obtained with $L_{\min} \geq 9$. However, the χ^2/DOF ratio for $L_{\min} = 6$ is still large, indicating the presence of subleading

TABLE IV. Results of the fits of $R = R_\xi$ to Eq. (21) (first three sets) and to Eq. (26) (last two sets) for the Kane-Mele-Hubbard model, with $U \in [5.625, 5.75]$. L_{min} is the minimum lattice size taken into account in the fits.

	L_{min}	U_c	ν	R_ξ^*	χ^2/DOF
	6	5.7524(4)	0.727(3)	0.26101(8)	4280.6/16
	9	5.7104(5)	0.716(5)	0.2516(2)	264.4/12
$n_{max} = 1$	12	5.711(1)	0.77(1)	0.2517(6)	217.5/8
	15	5.713(3)	0.84(4)	0.254(2)	195.3/4
	6	5.7335(3)	0.587(3)	0.26097(6)	2555.9/15
	9	5.7155(5)	0.657(5)	0.2526(2)	16.5/11
$n_{max} = 2$	12	5.7157(9)	0.68(1)	0.2528(5)	6.1/7
	15	5.716(2)	0.714(29)	0.253(2)	2.9/3
	6	5.7315(4)	0.615(3)	0.26072(7)	2471.3/14
	9	5.7147(6)	0.647(6)	0.2525(2)	9.8/10
$n_{max} = 3$	12	5.7155(9)	0.672(15)	0.2528(5)	5.4/6
	15	5.716(2)	0.715(35)	0.253(2)	2.9/2
$n_{max} = 2$	6	5.6982(9)	0.665(3)	0.2258(7)	140.0/14
$m_{max} = 0$	9	5.715(2)	0.659(6)	0.251(3)	16.4/10
$\omega = 0.785$	12	5.711(8)	0.69(2)	0.244(16)	5.8/6
$n_{max} = 3$	6	5.6976(9)	0.649(4)	0.2261(7)	107.8/13
$m_{max} = 0$	9	5.715(2)	0.646(7)	0.253(3)	9.7/9
$\omega = 0.785$	12	5.712(8)	0.68(2)	0.246(17)	5.2/5

scaling corrections. For $L_{min} \geq 9$, the fits to Eq. (26) exhibit χ^2/DOF ratios that are comparable to those obtained without scaling corrections. In particular, for $n_{max} = 2$ and $L_{min} = 9$ the fits to Eq. (26) still show a somewhat large χ^2/DOF ratio, suggesting either the presence of residual scaling corrections that are not taken into account by the present analysis, or that the Taylor expansion with $n_{max} = 2$ does not describe the data for $U \in [5.625, 5.75]$ and $L \leq 9$ in a fully reliable way. Nevertheless, the fitted values of U_c, ν, and R_ξ^* are essentially stable for $L_{min} \geq 9$, and upon including a correction-to-scaling term in the FSS analysis. By conservatively judging the fit results, we obtain the estimates

$$U_c = 5.71(1), \tag{30}$$

$$\nu = 0.68(3), \tag{31}$$

$$R_\xi^* = 0.250(6). \tag{32}$$

The estimates for U_c and ν have been chosen so to agree with the results of Table IV for $n_{max} \geq 2$ and $L_{min} = 9, 12$, including a variation of one error bar, with and without taking into account scaling corrections. They are also in agreement with the fit results for $L_{min} = 15$. The estimate for R_ξ^* has been chosen such that it agrees with the results of the fits that neglect scaling corrections for $n_{max} \geq 2$ and $L_{min} = 9, 12$, and with the results of the fits that consider scaling corrections for $n_{max} \geq 2$ and $L_{min} = 9$, including a variation of one error bar. The quoted value of R_ξ^* is also in agreement with the central value of the fits for $n_{max} \geq 2$, $m_{max} = 0$, and $L_{min} = 12$, and with the fits done without taking into account

TABLE V. Results of the fit of χ for the Kane-Mele-Hubbard model to Eq. (23) (first three sets) and to Eq. (33) (last set), with $R = R_\xi$ and $R_\xi \in [0.197, 0.287]$. L_{min} is the minimum lattice size taken into account.

	L_{min}	η'	χ^2/DOF
	6	0.003(1)	305.5/17
$n_{max} = 1$	9	0.059(4)	10.1/12
	12	0.071(9)	5.5/8
	6	0.003(1)	305.2/16
$n_{max} = 2$	9	0.068(5)	2.9/11
	12	0.08(1)	0.22/7
	6	0.003(1)	299.8/15
$n_{max} = 3$	9	0.068(5)	2.9/10
	12	0.08(1)	0.17/6
$n_{max} = 2$	6	0.087(8)	194.9/15
$m_{max} = 0$	9	0.076(21)	2.7/10
$\omega = 0.785$			

corrections to scaling, for $L_{min} \geq 15$. The final estimate of U_c is only in marginal agreement with the estimate obtained by a extrapolating the pseudocritical coupling $U_{c,R_{\xi,s,1/3,1/3}}(L)$. Such a difference does not contradict the precision of our final result for U_c because, as discussed above, the extrapolation of $U_{c,R_{\xi,s,1/3,1/3}}(L)$ may be affected by a systematic error.

In Table V, we report the results of the fits of χ to Eq. (23) for $R = R_\xi$. We restrict the analysis to the interval $R_\xi \in [0.197, 0.287]$, which for lattice sizes $L = 9 - 15$ corresponds to the interval $U \in [5.625, 5.75]$ that we used to analyze the
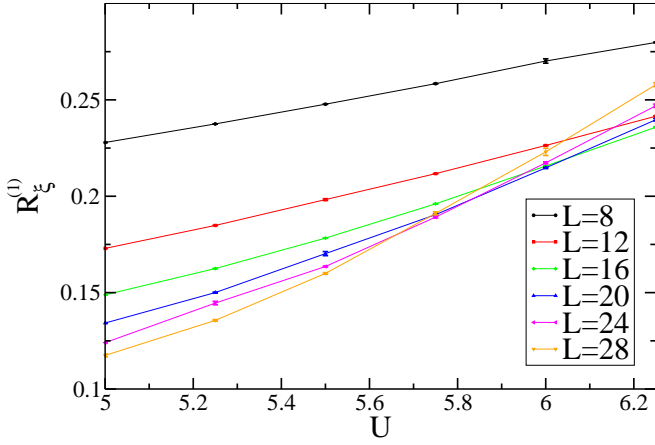
FIG. 10. (Color online) RG-invariant quantity $R_\xi^{(1)}$ for the π-flux Hubbard model. Lines are guides to the eye.

FIG. 11. (Color online) Same as Fig. 10 for $R_\xi^{(2)}$.

FSS behavior of R_ξ. We observe a small decrease of the χ^2/DOF ratio when we increase the expansion order from $n_{\max} = 1$ to $n_{\max} = 2$, while no appreciable difference is found upon further increasing $n_{\max}$ to $n_{\max} = 3$. The fits for $L_{\min} \geq 9$ exhibit a good χ^2/DOF ratio, and the fitted value of η' is stable upon increasing $L_{\min}$ and $n_{\max}$. As done for the FSS analysis of R_ξ, in order to monitor the role of the corrections to scaling, we repeated the fits including a correction-to-scaling term. We fitted the data of χ to

$$\chi(R, L) = L^{1-\eta'} \left(\sum_{n=0}^{n_{\max}} a_n R^n + L^{-\omega} \sum_{m=0}^{m_{\max}} b_m R^m \right), \quad (33)$$
$$\eta' \equiv \eta + z - 1,$$

using $\omega = 0.785$. By conservatively judging the variation of the results in Table V, we estimate

$$\begin{aligned} \eta' = \eta + z - 1 &= 0.075(20), \\ \eta &= 0.075(20) \quad (\text{if } z = 1), \end{aligned} \quad (34)$$

where the error bar essentially includes the estimates of all the fits. This value differs from the expected η exponent of the 3D XY UC, $\eta = 0.0381(2)$ [45]. Although the difference is within two error bars, it suggests the presence of residual scaling corrections that are not fully taken into account by the present analysis.

C. π-flux Hubbard model

We carried out QMC simulations of the π-flux Hubbard model for lattice sizes $L = 8$, 12, 16, 20, 24, and 28. In Figs. 10-13 we show the RG-invariant quantities $R_\xi^{(1)}$, $R_\xi^{(2)}$, $R_{\xi,s,1/2,1/2}$, and $R_{\xi,s,1/2,1/4}$, respectively, as a function of U and for different lattice sizes L. Inspection of Figs. $10-13$ reveals that $R_\xi^{(1)}$, $R_\xi^{(2)}$, $R_{\xi,s,1/2,1/2}$ are affected by significant scaling corrections, while reduced corrections to scaling are observed for the RG-invariant observable $R_{\xi,s,1/2,1/4}$. This observation is confirmed by the analysis of the pseudocritical
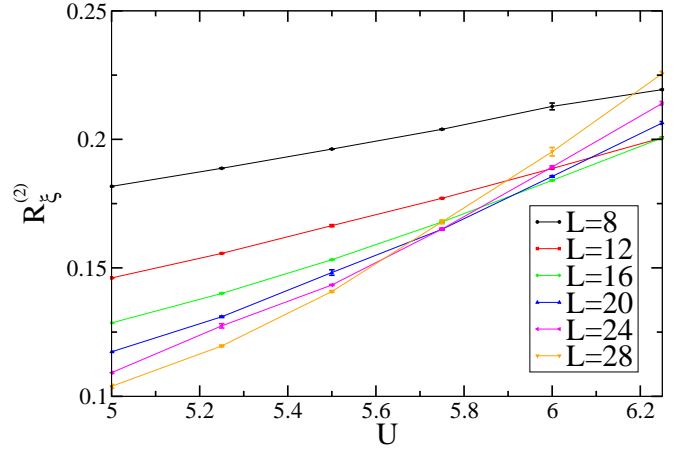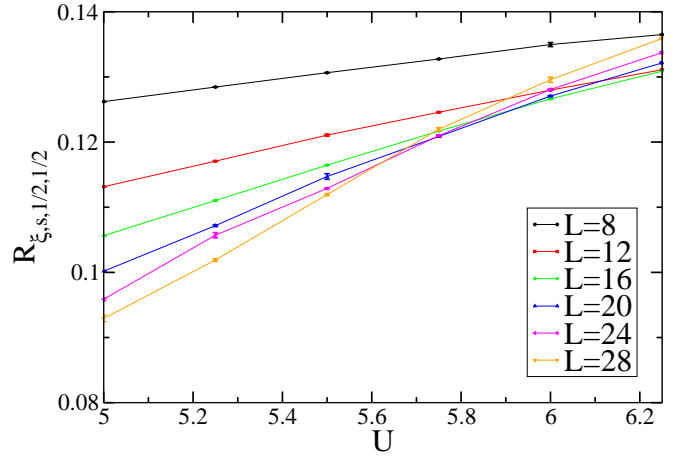

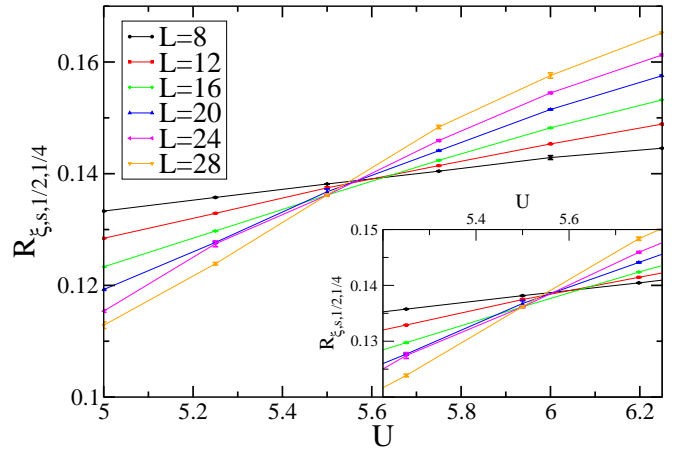FIG. 12. (Color online) Same as Fig. 10 for $R_{\xi,s,1/2,1/2}$.

FIG. 13. (Color online) Same as Fig. 10 for $R_{\xi,s,1/2,1/4}$. Inset: magnification of the data close to their crossing at $U \approx 5.5$.
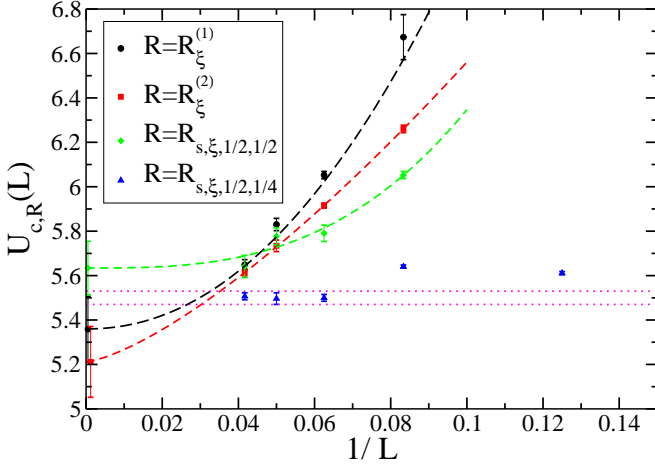
FIG. 14. (Color online) pseudocritical coupling $U_{c,R}$ for the π-flux Hubbard model and RG-invariant quantities $R = R_\xi^{(1)}$, $R_\xi^{(2)}$, $R_{\xi,s,1/2,1/2}$, and $R_{\xi,s,1/2,1/4}$. The dashed lines represent the right-hand side of Eq. (19), with the central values of the parameters as obtained by a fit to the right-hand side of Eq. (19) and reported in Table VI. For $R = R_\xi^{(1)}$, $R_\xi^{(2)}$, $R_{\xi,s,1/2,1/2}$, we also plot the extrapolated value of $U_{c,R}(L)$ for $L \to \infty$. The dotted lines indicate the interval in the final estimate of the critical coupling $U = 5.50(3)$ as reported in Eq. (35).

couplings. In Fig. 14, we show $U_{c,R}(L)$ as a function of $1/L$, as obtained by numerically solving Eq. (18), with $R = R_\xi^{(1)}$, $R_\xi^{(2)}$, $R_{\xi,s,1/2,1/2}$, $R_{\xi,s,1/2,1/4}$ and setting $c = 4$. For the RG-invariant quantities $R = R_\xi^{(1)}$, $R_\xi^{(2)}$, $R_{\xi,s,1/2,1/2}$, which exhibit significant scaling corrections, we fitted the resulting pseudocritical couplings $U_{c,R}(L)$ for $L = 12, 16, 20$, and 24 to Eq. (19), leaving U_c, A, and e as free parameters. The fit results reported in Table VI reveal a significant scatter in the extrapolated U_c. Moreover, the $\chi^2/$DOF is in most cases large, suggesting that these RG-invariant quantities are affected by a superposition of competing scaling corrections that are not captured by Eq. (19) where only the leading scaling correction has been taken into account. Moreover, for some of the RG-invariant observables considered here, the crossing between the lattice sizes $L = 12$ and $L = 16$ lies outside the range of the available MC data. In this case, the pseudocritical coupling has been obtained by extrapolating the values of R; such a procedure may introduce a bias, which can contribute to the observed spread in the extrapolated critical coupling U_c. The lack of larger lattice sizes does not allow us to further investigate these issues. On the other hand, the pseudocritical couplings $U_{c,R}(L)$ for $R = R_{\xi,s,1/2,1/4}$ appear to converge fast to U_c. Indeed, for $L \geq 16$, $U_{c,R}(L)$ is stable within error bars, suggesting $U_c \simeq 5.5$.

Since the RG-invariant quantity $R_{\xi,s,1/2,1/4}$ appears to have reduced scaling corrections, we analyzed its FSS behavior to determine the critical coupling U_c and the exponent ν. Similar to the analysis in Secs. V A and V B, we considered the QMC data in the interval $U \in [5.25, 6]$ around the observed common crossing of $R_{\xi,s,1/2,1/4}$ at $U \simeq 5.5$ for

TABLE VI. Results of fits of the pseudocritical couplings $U_{c,R}(L)$ to Eq. (19) for the RG-invariant observables $R = R_\xi^{(1)}$, $R_\xi^{(2)}$, $R_{\xi,s,1/2,1/2}$.

R	U_c	e	$\chi^2/$DOF
$R_\xi^{(1)}$	5.36(15)	2.1(6)	1.8
$R_\xi^{(2)}$	5.21(16)	1.4(3)	0.05
$R_{\xi,s,1/2,1/2}$	5.63(12)	2.9(1.8)	3.01

$L \geq 16$. For this data set, we fitted $R_{\xi,s,1/2,1/4}$ to Eq. (21). In Table VII, we report the fit results for different expansion orders $n_{\max}$ and minimum lattice sizes $L_{\min}$.

The ratio $\chi^2/$DOF decreases significantly upon increasing $n_{\max}$ from $n_{\max} = 1$ to $n_{\max} = 2$, and only marginally between $n_{\max} = 2$ and $n_{\max} = 3$. This suggests that the Taylor expansion with $n_{\max} = 2$ should be adequate in this interval of U. We find that $\chi^2/$DOF decreases upon increasing $L_{\min}$, but remains large even for the largest $L_{\min}$ used. This implies that, within the available numerical precision, scaling corrections are important. The limited number of data points does not allow for a more precise analysis, e.g., by including corrections to scaling as done in Sec. V A (only four points are available for each L in the chosen interval). Nevertheless, Table VII reveals that for $n_{\max} \geq 2$, the fitted value of U_c appears to be stable for $L_{\min} \geq 16$, and the fitted exponent ν is essentially in agreement with the estimate for the honeycomb Hubbard model, $\nu = 0.84(4)$ [Eq. (28)]. Similar results are found by analyzing the data in a smaller interval $U \in [5.25, 5.75]$ and setting $n_{\max} = 1$. The corresponding fit results are reported in Table VIII. Given the difficulty in studying the FSS of $R_{\xi,s,1/2,1/4}$, we determined U_c on the basis of the pseudocritical couplings $U_{c,R}(L)$ as computed for $R = R_{\xi,s,1/2,1/4}$. As mentioned above, $U_{c,R}(L)$ for $R = R_{\xi,s,1/2,1/4}$ is stable within error bars for $L \geq 16$: we find $U_{c,R}(L = 16) = 5.50(2)$, $U_{c,R}(L = 20) = 5.50(3)$, $U_{c,R}(L = 24) = 5.51(2)$. Based on these values, we arrive at the estimate

$$U_c = 5.50(3), \qquad (35)$$

where the error bar is chosen so that U_c agrees with $U_{c,R}(L)$ for $R = R_{\xi,s,1/2,1/4}$ and $L \geq 16$, including a variation of one standard variation.

To further strengthen the hypothesis that the critical behavior belongs to the same UC as for the honeycomb Hubbard model, we produced a scaling collapse for $R_{\xi,s,1/2,1/4}$. Using the value of U_c given in Eq. (35) and the estimate of ν given in Eq. (28), we plot in Fig. 15 $R_{\xi,s,1/2,1/4}$ as a function of the scaling variable w defined in Eq. (10). Within the error bars, the data show a collapse, consistent with the idea that the critical behavior belongs to the Gross-Neveu-Heisenberg UC; the largest contribution to the error bars on w is due to the uncertainty on the exponent ν, which is responsible for the large error bars of the largest lattice sizes.

In Table IX, we report the results of fits of χ to Eq. (23) for $R = R_{\xi,s,1/2,1/4}$, in the interval $R_{\xi,s,1/2,1/4} \in [0.123, 0.15]$ corresponding to $U \in [5.25, 5.75]$ for $L \geq 20$, to $U \in [5, 6]$

TABLE VII. Same as Table I for $R = R_{\xi,s,1/2,1/4}$ and the π-flux Hubbard model, with $U \in [5.25, 6]$.

	$L_{\min}$	U_c	ν	$R^*_{\xi,s,1/2,1/4}$	$\chi^2/$DOF
$n_{\max} = 1$	8	5.601(2)	0.777(4)	0.13899(3)	976.5/20
	12	5.561(3)	0.836(7)	0.13796(6)	438.4/16
	16	5.507(5)	0.93(2)	0.1363(1)	117.2/12
	20	5.50(1)	0.91(3)	0.1361(4)	88.9/11
$n_{\max} = 2$	8	5.592(2)	0.768(4)	0.13892(3)	914.2/19
	12	5.554(3)	0.819(7)	0.13792(6)	383.0/15
	16	5.495(5)	0.888(14)	0.1361(1)	22.7/11
	20	5.49(1)	0.90(3)	0.1359(4)	21.4/7
$n_{\max} = 3$	8	5.594(2)	0.724(6)	0.13890(3)	842.0/18
	12	5.556(3)	0.782(9)	0.13791(6)	360.4/14
	16	5.498(4)	0.85(2)	0.1361(1)	16.7/10
	20	5.49(1)	0.85(4)	0.1357(4)	16.1/6

TABLE VIII. Same as Table VII for $U \in [5.25, 5.75]$ and $n_{\max} = 1$.

$L_{\min}$	U_c	ν	$R^*_{\xi,s}$	$\chi^2/$DOF
8	5.596(2)	0.765(6)	0.13898(3)	867.4/14
12	5.556(3)	0.806(9)	0.13792(7)	356.3/11
16	5.503(4)	0.87(2)	0.1362(1)	20.7/8
20	5.49(1)	0.85(4)	0.1356(4)	14.7/5
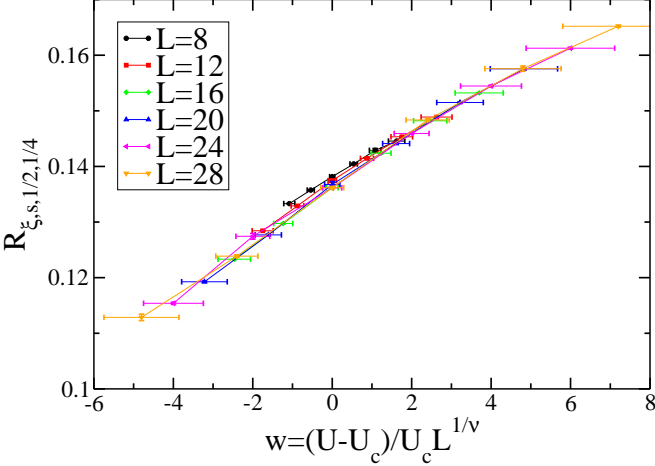
FIG. 15. (Color online) Scaling collapse for the RG-invariant quantity $R_{\xi,s,1/2,1/4}$ for the π-flux Hubbard model. Lines are guides to the eye. The scaling variable w is computed using U_c as given in Eq. (35) and ν as reported in Eq. (28).

TABLE IX. Same as Table III for the π-flux Hubbard model for $R = R_{\xi,s,1/2,1/4}$, with $R_{\xi,s,1/2,1/4} \in [0.123, 0.15]$.

	$L_{\min}$	η'	$\chi^2/$DOF
$n_{\max} = 1$	8	0.649(2)	4373.9/23
	12	0.681(3)	2312.2/17
	16	0.711(7)	692.1/11
	20	0.71(2)	80.3/6
$n_{\max} = 2$	8	0.679(2)	768.4/22
	12	0.670(3)	239.5/16
	16	0.696(7)	43.0/10
	20	0.70(2)	2.1/5
$n_{\max} = 3$	8	0.679(2)	765.9/21
	12	0.668(4)	236.6/15
	16	0.697(7)	30.3/9
	20	0.71(2)	0.23/4
$n_{\max} = 2$ $m_{\max} = 1$	8	0.92(2)	104.9/20
	12	1.14(7)	32.6/14
	16	0.99(20)	7.7/8

for $L = 16$, and to $U \in [5, 6.25]$ for $L \leq 12$. We observe that $\chi^2/$DOF decreases significantly between $n_{\max} = 1$ and $n_{\max} = 2$, while a much smaller change is found between $n_{\max} = 2$ and $n_{\max} = 3$. The value of $\chi^2/$DOF decreases upon disregarding the smallest lattice size, but remains large even for $L_{\min} = 20$, signaling the importance of scaling corrections. Indeed, the fitted value of η' is large, $\eta' \sim 0.7$, which, analogous to the honeycomb Hubbard model, implies

the presence of slowly-decaying scaling corrections (compare with Table III). As for the honeycomb Hubbard model, we attempted to take into account these scaling corrections by including a background term. The results of a fit of $R_{\xi,s,1/2,1/4}$ to Eq. (24) using $n_{\max} = 2$ and $m_{\max} = 1$ are given in Table IX. The fitted values of η' do not exhibit stability, and a small value of $\chi^2/$DOF is found for $L_{\min} = 16$ only; in this case the fitted value of η' agrees within error bars with the

estimate for the honeycomb Hubbard model [Eq. (25)]. The available data points do not allow for a more detailed analysis. Nevertheless, there is little doubt that η' (and hence η, assuming $z = 1$) is large, consistent with the Gross-Neveu-Heisenberg UC.

VI. SUMMARY

We investigated the critical behavior of the honeycomb and the π-flux Hubbard model, as well as the Kane-Mele-Hubbard model. Our main findings are as follows.

(i) By means of a FSS analysis that exploits RG-invariant observables, we determined the value of the critical coupling [Eq. (27))] and an estimate of the critical exponents ν [Eq. (28)] and η [Eq. (25)] for the Hubbard model on the honeycomb lattice (see Sec. V A). The critical exponents are consistent with Gross-Neveu-Yukawa theory, in particular with a summation of the ε-expansion to the first loop that gives $\nu = 97/110 \simeq 0.88$, $\eta = 0.8$. This justifies *a posteriori* the use of these critical exponents to obtain a scaling collapse in a previous QMC study of the honeycomb Hubbard model [13], and of the Kane-Mele-Coulomb model [30] for which the long-range Coulomb repulsion is expected to be marginally irrelevant [46]. On the other hand, our determination of the critical exponents is not compatible with recent functional RG results [42]. Our U_c is in line with the value $U_c \simeq 3.78$ reported in Ref. [13].

(ii) Most notably, the critical behavior of the Hubbard model on the honeycomb lattice is characterized by a large value of the η exponent. As a consequence, the singular part of the two-point function of the order parameter decays fast as a function of the distance, so that the short-distance nonuniversal behavior gives a significantly large contribution to the spatial correlations. This results in slowly-decaying corrections to scaling that originate from the analytic part of the free energy and are characterized by a small effective correction-to-scaling exponent $\omega = 0.30(15)$ [see the discussion after Eq. (25)]. For comparison, for 3D classical $O(N)$ models $\eta \lesssim 0.04$, so that the leading scaling correction is due to the leading irrelevant operator, with $\omega \approx 0.8$ [38]. Examples of classical models affected by slowly decaying scaling corrections are the 3D site-dilute and bond-dilute Ising models, where $\omega = 0.33(3)$ [43]; for this UC the currently most precise critical exponents were obtained by simulating a classical 3D spin model with a lattice size up to $L = 192$ [43]. The presence of slowly-decaying scaling corrections in the Gross-Neveu-Heisenberg UC hinders a precise determination of the exponent η.

(iii) We analyzed the critical behavior of the Kane-Mele-Hubbard model with spin-orbit coupling $\lambda = 0.2$ (see Sec. V B), including a determination of the critical coupling [Eq. (30)] and the critical exponents ν [Eq. (31)] and η [Eq. (34)]. The analysis confirms that the critical behavior belongs to the 3D XY UC, whose critical exponents are $\nu = 0.6717(1)$, $\eta = 0.0381(2)$ [45]. For this UC, the leading corrections to scaling are due to the leading irrelevant operator, whose negative RG-dimension is $\omega = 0.785(20)$

[45]. Assuming that the realization of the 3D XY UC by the Kane-Mele-Hubbard model does not generate additional irrelevant operators with a smaller negative RG-dimension, $\omega = 0.785(20)$ [45] should characterize the leading scaling corrections [cf. the Hubbard model, where $\omega = 0.30(15)$, see discussion after Eq. (25)]. Our analysis of the η exponent shows a small deviation, less than two error bars, from the precise determination for the 3D XY UC $\eta = 0.0381(2)$ [45], suggesting the presence of residual scaling corrections that are not fully taken into account by the present analysis.

(iv) We analyzed the critical behavior of the π-flux Hubbard model (see Sec. V C). Although the available MC data do not allow for an independent determination of the critical exponents, we provided evidence that the critical behavior is consistent with the Gross-Neveu-Heisenberg UC.

(v) Using the notion of a pseudocritical coupling (cf. discussion at the end of Sec. III) we determined the value of the critical coupling U_c [Eq. (35)] for the π-flux Hubbard model. A comparison with the corresponding value for the Hubbard model shows an interesting relation between the two critical couplings. By rescaling the values of U_c [Eqs. (27) and (35)] with the geometric average of the velocities at the Dirac cones [Eq. (4)], we obtain

$$\frac{U_c}{\sqrt{v_x v_y}} \simeq 4.4 \quad \text{(honeycomb Hubbard model)},$$
$$\frac{U_c}{\sqrt{v_x v_y}} \simeq 4.2 \quad (\pi\text{-flux Hubbard model}). \tag{36}$$

These results suggest that the velocities at the Dirac cones are the main contribution to the renormalization of U_c. Note that the bandwidth W is similar (but not equal) in the two models: $W = 6$ for the honeycomb Hubbard model, and $W = 4\sqrt{2} \simeq 5.6$ for the π-flux Hubbard model [15]. The residual difference in the ratios in Eq. (36) may originate from the ratio of the two bandwidths.

(vi) In this work, we studied the critical behavior of the magnetic order parameter only. Recent studies of the honeycomb Hubbard model [13] and of the π-flux Hubbard model [15] provided evidence that the opening of the single particle gap coincides with the onset of antiferromagnetic order. Together with these results, our analysis supports the validity of the Gross-Neveu-Yukawa theory, which predicts that the fermionic and bosonic degrees of freedom become critical at the same value of U_c, resulting in a direct transition between a semimetallic phase and an antiferromagnetic state.

(vii) Our FSS analysis exploited RG-invariant observables defined as ratios ξ/L of the finite-size correlation length ξ and the system size L. In a finite system, there is no unique definition of ξ, and we defined several correlation lengths that are inequivalent in the FSS limit (see Appendix A). This freedom in the definition of ξ leads us to several RG-invariant observables, some of them approximately improved, i.e., showing significantly reduced scaling corrections. Improved observables and improved models are instrumental in high-precision studies of critical phenomena [38].

Appendix A: Finite-size correlation length

1. Regular lattices

On an infinite lattice with dimension d, the second-moment correlation length ξ is defined as

$$\xi^2 \equiv \frac{1}{2d} \frac{\sum_{\vec{x}} |\vec{x}|^2 C(\vec{x})}{\sum_{\vec{x}} C(\vec{x})}, \quad \text{(A1)}$$

where the sum is over the points $\vec{x}$ on the lattice, $C(\vec{x})$ is the two-point function of the order parameter, and $|\vec{x}|$ is the Euclidean length of the vector $\vec{x}$. Here we assume that the order parameter is a local quantity defined in terms of the observables on a single lattice site $\vec{x}$. Equation (A1) can be written as

$$\xi^2 = -\frac{1}{2d\widetilde{C}(\vec{p}=0)} \sum_i \frac{\partial^2 \widetilde{C}(\vec{p})}{\partial p_i \partial p_i}\bigg|_{\vec{p}=0}, \quad \text{(A2)}$$

where $\widetilde{C}(\vec{p})$ is the Fourier transform of $C(\vec{r})$,

$$\widetilde{C}(\vec{p}) \equiv \sum_{\vec{r}} e^{i\vec{p}\vec{r}} C(\vec{r}), \quad \text{(A3)}$$

and the derivatives of $\widetilde{C}(\vec{p})$ in Eq. (A2) are taken with respect to the Euclidean basis, or with respect to another orthonormal basis. In the following, we specialize the discussion to the case $d = 2$, i.e., of a two-dimensional lattice. An extension to higher-dimensional lattices is straightforward.

In a finite lattice with size L there is not a unique definition of ξ, but, in the presence of periodic boundary conditions one can substitute the derivative in Eq. (A2) with a finite incremental ratio calculated on the smallest momentum of the lattice $p_{\min} \sim 1/L$. To this end, we first analyze the proper-

ties of the Taylor expansion of $\widetilde{C}(\vec{p})$ for $\vec{p} \to 0$ [2]:

$$\widetilde{C}(\vec{p}) = \widetilde{C}(0) + g_x p_x + g_y p_y + g_{xx} p_x^2 + g_{xy} p_x p_y + g_{yy} p_y^2 + O(p^4), \quad \text{(A4)}$$

where p_x, p_y are the components of $\vec{p}$ in the Euclidean basis (in general not coinciding with the reciprocal lattice basis). The symmetries of the lattice constrain the coefficients g_i, g_{ij} in Eq. (A4). In fact, the invariance under a rotation by an angle θ, described by

$$\begin{pmatrix} p_x \\ p_y \end{pmatrix} \to \begin{pmatrix} \cos\theta & -\sin\theta \\ \sin\theta & \cos\theta \end{pmatrix} \begin{pmatrix} p_x \\ p_y \end{pmatrix} \quad \text{(A5)}$$

with $\theta \neq 0, \pi$ requires the coefficients to satisfy

$$g_x = g_y = g_{xy} = 0, \quad g_{xx} = g_{yy} \equiv A, \quad \text{(A6)}$$

so that Eq. (A4) can be simplified to

$$\widetilde{C}(\vec{p}) = \widetilde{C}(0) + A \left(p_x^2 + p_y^2 \right) + O(p^4). \quad \text{(A7)}$$

Equation (A7) holds, in particular, for the square lattice ($\theta = \pi/2$) and for the triangular lattice ($\theta = 2\pi/3$). By inserting Eq. (A7) in Eq. (A2), we find ($d = 2$)

$$\xi^2 = -\frac{A}{\widetilde{C}(0)}, \quad \text{(A8)}$$

so that the expansion of Eq. (A7) can be expressed as

$$\widetilde{C}(\vec{p}) = \widetilde{C}(0) \left[1 - \xi^2 \left(p_x^2 + p_y^2 \right) \right] + O(p^4). \quad \text{(A9)}$$

Then, for any function $\Delta(\vec{p})$ that has a Taylor expansion of the form

$$\Delta(\vec{p}) = p_x^2 + p_y^2 + O(p^4), \quad \text{(A10)}$$

we find that

$$\frac{1}{\Delta(\vec{p})} \left[\frac{\widetilde{C}(0)}{\widetilde{C}(\vec{p})} - 1 \right] = \xi^2 + O(p^2), \qquad \vec{p} \to 0. \quad \text{(A11)}$$

This result suggests to define, on a *finite* lattice with size L, the correlation length $\xi(L)^2$ as

$$\xi(L)^2 \equiv \frac{1}{\Delta(\vec{p}_{\min})} \left[\frac{\widetilde{C}(0)}{\widetilde{C}(\vec{p}_{\min})} - 1 \right], \quad \text{(A12)}$$

where $\vec{p}_{\min}$ is the minimum momentum on a lattice of size L. In a two-dimensional lattice there are two such minimum

---

[2] Even if the Fourier transform $\widetilde{C}(\vec{p})$ is not analytic, we can still regard the expansion of Eq. (A4) as describing the small-momentum behavior of a system with a large but finite size L, where the smallest momentum of the lattice $p_{\min} \sim 1/L$. In fact, all we need for the FSS analysis is to provide a definition of ξ such that the ratio ξ/L is RG-invariant and the finite-size correlation length $\xi(L)$ is analytic in an interval around the critical point.

momenta where, by virtue of the lattice symmetry, $\widetilde{C}(\vec{p})$ takes the same value. For simplicity, in Eq. (A12), we neglected a possible dependence of $\xi(L)$ on additional parameters of the model, such as the Hubbard coupling U or the temperature. A comparison of Eq. (A11) with Eq. (A2) shows that for $L \to \infty$ the finite-size correlation length $\xi(L)$ coincides with the second-moment correlation length ξ up to corrections of order $\sim p_{\min}^2 \sim 1/L^2$.

The choice of $\Delta(\vec{p})$ to be used in Eq. (A12) is usually dictated by the solution of a Gaussian model on the same lattice. For such a model the Fourier transform of the two-point function can be determined as

$$\widetilde{C}(\vec{p}) = \frac{\widetilde{C}(0)}{1 + \xi^2 \Delta(\vec{p})}, \qquad (A13)$$

where the function $\Delta(\vec{p})$ depends on the lattice, its normalization is fixed by Eq. (A10) and, in agreement with Eq. (A9), the coefficient in front of $\Delta(\vec{p})$ is equal to the second-moment correlation length. Inverting Eq. (A13), we find that for a Gaussian model ξ is exactly given by

$$\xi^2 = \frac{1}{\Delta(\vec{p})} \left[\frac{\widetilde{C}(0)}{\widetilde{C}(\vec{p})} - 1 \right]. \qquad (A14)$$

For an interacting model on a finite regular lattice, we can use the definition of Eq. (A12) for the finite-size correlation length $\xi(L)$ and replace $\Delta(\vec{p})$ with the function obtained for the Gaussian model on the same lattice. With this choice, the definition of Eq. (A12) gives exactly the second-moment correlation length in the case of a Gaussian model. A different choice of $\Delta(\vec{p})$, with the same normalization of Eq. (A10), would give rise to different corrections $\propto 1/L^2$, which are in any case negligible compared to the leading scaling correction.

For a square lattice, the function $\Delta(\vec{p})$ is

$$\Delta(\vec{p}) = 4 \left[\sin\left(\frac{p_x}{2}\right)^2 + \sin\left(\frac{p_y}{2}\right)^2 \right]. \qquad (A15)$$

The direct lattice basis $\{\vec{a}_1, \vec{a}_2\}$ and the reciprocal one $\{\vec{b}_1, \vec{b}_2\}$ of the square lattice are

$$\vec{a}_1 = \begin{pmatrix} 1 \\ 0 \end{pmatrix}, \ \vec{a}_2 = \begin{pmatrix} 0 \\ 1 \end{pmatrix}, \quad \vec{b}_1 = \begin{pmatrix} 0 \\ 1 \end{pmatrix}, \ \vec{b}_2 = \begin{pmatrix} 1 \\ 0 \end{pmatrix}, \quad (A16)$$

where the lattice constant has been set to 1 and the basis has been normalized such that

$$\vec{a}_i \cdot \vec{b}_j = \delta_{ij}. \qquad (A17)$$

On a finite lattice with size L, the two minimum momenta are $\vec{p}_{\min} = (2\pi/L)\vec{b}_1 = (2\pi/L, 0)$ and $\vec{p}_{\min} = (2\pi/L)\vec{b}_2 = (0, 2\pi/L)$. For these momenta, $\Delta(\vec{p})$ takes the value

$$\Delta(\vec{p}_{\min}) = 4 \sin(\pi/L)^2. \qquad (A18)$$

For a triangular lattice, the function $\Delta(\vec{p})$ is reported in Appendix A of Ref. [47]:

$$\Delta(\vec{p}) = 4 \left[1 - \frac{1}{3} \left(\cos(p_x) + 2 \cos\left(\frac{p_x}{2}\right) \cos\left(\frac{\sqrt{3} p_y}{2}\right) \right) \right]. \qquad (A19)$$
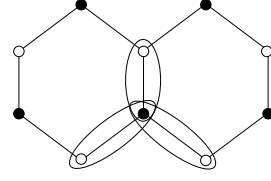

FIG. 16. A portion of a honeycomb lattice, which can be considered as a triangular lattice with a unit cell of two sites. The filled (empty) circles are sites on the A (B) sublattice. The ellipses indicate three possible choices for the unit cell. Rotations by $\theta = 2\pi/3$ map the possible choices for the unit cell onto each other.

The direct and reciprocal bases of the triangular lattice are

$$\vec{a}_1 = \begin{pmatrix} 1 \\ 0 \end{pmatrix}, \ \vec{a}_2 = \begin{pmatrix} \frac{1}{2} \\ \frac{\sqrt{3}}{2} \end{pmatrix}, \quad \vec{b}_1 = \begin{pmatrix} 1 \\ -\frac{1}{\sqrt{3}} \end{pmatrix}, \ \vec{b}_2 = \begin{pmatrix} 0 \\ \frac{2}{\sqrt{3}} \end{pmatrix}, \qquad (A20)$$

with the same normalization as in Eq. (A17). On a finite lattice with size L, the two minimum momenta are $\vec{p}_{\min} = (2\pi/L)\vec{b}_1 = (2\pi/L, -2\pi/\sqrt{3}/L)$ and $\vec{p}_{\min} = (2\pi/L)\vec{b}_2 = (0, 4\pi/\sqrt{3}/L)$. For these momenta, $\Delta(\vec{p})$ takes the value

$$\Delta(\vec{p}_{\min}) = \frac{16}{3} \sin(\pi/L)^2. \qquad (A21)$$

The fact that $\Delta(\vec{p})$ takes the same value for the two minimum momenta for both lattices considered here is a direct consequence of the invariance under the symmetry of Eq. (A5) with $\theta = \pi/2$ for the square lattice, and $\theta = 2\pi/3$ for the triangular lattice.

2. Honeycomb lattice

Since the honeycomb lattice can be considered as a triangular lattice where the elementary cell has two sites, the two-point function $C(\vec{x})$ of a local order parameter constructed on a single elementary unit cell can be defined so that its domain is a triangular lattice, i.e., $\vec{x} = n_1 \vec{a}_1 + n_2 \vec{a}_2$, with the lattice basis $\{\vec{a}_1, \vec{a}_2\}$ given in Eq. (A20). However, different than in the case of a triangular lattice, the two-point function $C(\vec{x})$ may not be invariant under the rotation of Eq. (A5) with $\theta = 2\pi/3$. In fact, such a symmetry holds for some choices of the order parameter only. If the local order parameter $\phi(\vec{x})$ in the unit cell $\vec{x}$ is defined in terms of observables at lattice site $\vec{x}_A$ ($\vec{x}_B$) that belongs to the A (B) sublattice, then effectively the two-point function $C(\vec{x})$ is invariant under the rotation group of the triangular lattice, i.e., the rotation of Eq. (A5) with $\theta = 2\pi/3$. For instance, this is the case when the order parameter is the A or B sublattice magnetization. In this work, we have considered the antiferromagnetic order parameters given in Eqs. (5) and (6). For these local order parameters, which involve a combination of the A and B sublattice magnetization, the two-point function $C(\vec{x})$ is not invariant under a rotation by $\theta = 2\pi/3$. The reason lies in the ambiguity in defining the elementary unit cell of the honeycomb lattice. As illustrated in Fig. 16, there are three possible

choices for defining the elementary unit cell; a rotation by $\theta = 2\pi/3$ maps one possible unit cell to another.

The absence of the lattice rotational symmetry for $C(\vec{x})$ requires a generalization of the arguments given in Appendix A 1. To this end, let us consider in full generality a finite lattice that extends over L_1 (L_2) lattice unit cells in the direction parallel to $\vec{a}_1$ ($\vec{a}_2$). For such a lattice, there are two minimum momenta

$$\vec{p}_{\min}^{(1)} = \frac{2\pi}{L_1}\vec{b}_1 = \left(\frac{2\pi}{L_1}, -\frac{2\pi}{\sqrt{3}L_1}\right), \qquad \text{(A22)}$$

$$\vec{p}_{\min}^{(2)} = \frac{2\pi}{L_2}\vec{b}_2 = \left(0, \frac{4\pi}{\sqrt{3}L_2}\right). \qquad \text{(A23)}$$

A straight-forward generalization of Eq. (A12) consists in defining a finite-size correlation length $\xi^{(i)}(L)$ for each principal direction $i = 1, 2$ as

$$\xi^{(i)}(L)^2 \equiv \frac{1}{\Delta(\vec{p}_{\min}^{(i)})}\left[\frac{\widetilde{C}(0)}{\widetilde{C}(\vec{p}_{\min}^{(i)})} - 1\right], \quad i = 1, 2, \quad \text{(A24)}$$

where $\Delta(\vec{p})$ is given in Eq. (A19). Even if, due to the lack of the lattice rotational symmetry, $\widetilde{C}(\vec{p}_{\min}^{(1)}) \neq \widetilde{C}(\vec{p}_{\min}^{(2)})$, for $L_1 = L_2 = L$ it is possible to define an averaged correlation length by taking the mean value of $\widetilde{C}(\vec{p})$ over the two minimum momenta:

$$\xi(L)^2 \equiv \frac{1}{\Delta(\vec{p}_{\min})}\left[\frac{\widetilde{C}(0)}{\left(\widetilde{C}(\vec{p}_{\min}^{(1)}) + \widetilde{C}(\vec{p}_{\min}^{(2)})\right)/2} - 1\right]. \quad \text{(A25)}$$

For $L_1 = L_2 = L$, $\Delta(\vec{p})$ takes the same value given in Eq. (A21) at the two minimum momenta $\vec{p}_{\min}^{(1)}$ and $\vec{p}_{\min}^{(2)}$ (see the discussion at end of Appendix A 1). The definition of $\xi(L)$ given in Eq. (A25) corresponds to a generalized f-mean value of $\xi^{(1)}(L)$ and $\xi^{(2)}(L)$,

$$\xi(L) = f^{-1}\left(\frac{f(\xi^{(1)}(L)) + f(\xi^{(2)}(L))}{2}\right), \qquad \text{(A26)}$$

where $f(x)$ is a monotonic positive function

$$f(x) = \frac{1}{1 + x^2 \Delta(\vec{p}_{\min})}. \qquad \text{(A27)}$$

Moreover, if $\xi^{(i)}/L$ are RG-invariant quantities, then ξ/L is also an RG-invariant observable.

3. Correlation length from real-space correlations

An alternative definition of the finite-size correlation length can be obtained by directly considering Eq. (A1) and extending the sum over the (finite) set of lattice sites. With periodic boundary conditions, such a prescription does not uniquely fix the definition of ξ. To be specific, as in Appendix A 2, we consider a finite lattice that extends over L_i lattice sites in the direction parallel to $\vec{a}_i$, with $i = 1, 2$. With

periodic boundary conditions, the two-point function satisfies $C(\vec{x}) = C(\vec{x} + nL_1\vec{a}_1 + mL_2\vec{a}_2)$ for arbitrary integers n and m. However, the Euclidean length $|\vec{x}|$ in Eq. (A1) is not invariant under translations. This leaves us the freedom to define the correlation length as a sum over $\vec{x} = n_1\vec{a}_1 + n_2\vec{a}_1$, where n_i runs over $-(L_i - 1) + l_i, -(L_i - 1) + l_i + 1, \ldots, l_i - 1, l_i$, with arbitrary l_i. In order to have a nontrivial FSS limit, the maximum value of the index l_i must be proportional to L_i.

These considerations lead us to define a finite-size correlation length $\xi_{s,\kappa,\rho}(L)$ as

$$\xi_{s,\kappa,\rho}(L)^2 \equiv \frac{\displaystyle\sum_{\substack{(-1+\kappa)L_1+1\leq n_1\leq\kappa L_1 \\ (-1+\rho)L_2+1\leq n_2\leq\rho L_2}} |n_1\vec{a}_1 + n_2\vec{a}_2|^2 C(n_1\vec{a}_1 + n_2\vec{a}_2)}{\displaystyle\sum_{\substack{0\leq n_1\leq L_1-1 \\ 0\leq n_2\leq L_2-1}} C(n_1\vec{a}_1 + n_2\vec{a}_2)}. \qquad \text{(A28)}$$

We note that, by virtue of the aforementioned translational invariance, in the denominator of Eq. (A28) a shift of the sum as done for the numerator does not change the result. In Eq. (A28), the choice of $\kappa = \rho = 1/2$ corresponds to defining the distance $|\vec{x}|$ as the minimum one.

Although in the infinite-volume limit $L_1, L_2 \to \infty$ *at fixed* U the correlation lengths as defined in Eqs. (A28) and (A12) converge to the same observable, in the FSS limit these definitions of ξ, as well as those given in Eqs. (A24) and (A25), correspond to different observables. As a consequence, the corresponding ratios ξ/L constructed with the various definitions of ξ [see Eqs. (11)–(15)] correspond to different RG-invariant quantities. This in particular affects the corrections to scaling which, as shown in Sec. V, can be significantly different. In particular, setting $\kappa = \rho = 0$ in Eq. (A28) gives rise to a large contribution of the numerator when $|\vec{x}| \approx L_1, L_2$ because, for such values of $\vec{x}$ and due to the periodic boundary conditions, $C(\vec{x}) \approx C(0)$. This results in a large background term due to the nonuniversal short-distance part of the correlation function that gives rise to large corrections to scaling.

Finally, we observe that Eq. (A28) is correctly defined only when κL_1 and ρL_2 are integer numbers. In order to be able to extrapolate to the FSS limit, this property must hold for every lattice size. Such limitations on the values of κ and ρ, together with the limitations on the lattice sizes that can be simulated (see Sec. IV), further limit the applicability of Eq. (A28) for generic values of κ and ρ. For the honeycomb Hubbard and the Kane-Mele-Hubbard models we simulated lattices with $L_1 = L_2 = L$, with L being a multiple of 3. For this reason, we employed the definition in Eq. (A28) with $\kappa = \rho = 1/3$. In the case of the π-flux Hubbard model, we simulated lattices with $L_1 = L/2$ and $L_2 = L$, with L being a multiple of 4. This leads us to either choose $\kappa = \rho = 1/2$ or $\kappa = 1/2$ and $\rho = 1/4$, the latter giving rise to smaller scaling corrections (see Sec. V C).

TABLE X. Results of the fit of χ for the honeycomb Hubbard model to Eq. (B1) (first three sets) and to Eq. (B2) (last two sets), for $U \in [3.6, 4]$. The critical exponent η' is defined as $\eta' \equiv \eta + z - 1$, with $\eta' = \eta$ if $z = 1$. $L_{\min}$ is the minimum lattice size taken into account in the fits. In the quoted error bars for η', the first number reports the statistical precision as obtained from the fit, while the second number gives the sum of the maximum variation in the results upon varying U_c and upon varying ν within one error bar, as quoted in Eqs. (27) and (28). The corresponding maximum oscillation of χ^2 is reported between parentheses after its central value.

	$L_{\min}$	η'	χ^2/DOF
	6	0.7154(8 + 79)	2832(985)/22
$n_{\max} = 1$	9	0.696(1 + 11)	1902(481)/17
	12	0.671(3 + 14)	894(107)/12
	6	0.7359(9 + 94)	644(519)/21
$n_{\max} = 2$	9	0.735(2 + 12)	383(271)/16
	12	0.731(4 + 13)	110(67)/11
	6	0.7324(9 + 85)	213(167)/20
$n_{\max} = 3$	9	0.731(2 + 11)	129(77)/15
	12	0.734(4 + 15)	45(20)/10
$n_{\max} = 2$	6	0.887(7 + 72)	142(87)/20
$m_{\max} = 0$	9	0.93(1 + 8)	24.2(10.3)/15
$n_{\max} = 2$	6	0.78(1 + 6)	84(29)/19
$m_{\max} = 1$	9	0.83(5 + 7)	19(6)/14
$n_{\max} = 2$	6	0.79(2 + 5)	80(31)/18
$m_{\max} = 2$	9	0.79(5 + 6)	17.3(3.4)/13

Appendix B: Finite-size scaling analysis of χ at fixed U for the honeycomb Hubbard model

In order to further assess the reliability of the results of Sec. V A and the overall consistency of the estimates of the critical exponents for the honeycomb Hubbard model, we analyzed the FSS behavior of χ as a function of U and L, as we did for the RG-invariant quantity $R_{\xi,s,1/3,1/3}$. To this end, we consider a Taylor expansion of the right-hand side of Eq. (9). Neglecting scaling corrections, we fit our data for χ to

$$\chi(U, L) = L^{1-\eta'} \sum_{n=0}^{n_{\max}} a_n (U - U_c)^n L^{n/\nu}, \qquad \text{(B1)}$$

leaving η', $\{a_n\}$ as free parameters, and using the values of U_c and ν as given by Eqs. (27) and (28). We repeat the fit by varying U_c and ν within one error bar as quoted in Eqs. (27) and (28). As in the FSS analysis of $R_{\xi,s,1/3,1/3}$, we restrict the analysis to values $U \in [3.6, 4]$ and systematically disregard the smallest lattice sizes. The fit results are reported in Table X. Inspection of the results reveals a significant decrease of the χ^2/DOF ratio when we increase $n_{\max}$ from $n_{\max} = 1$ to $n_{\max} = 2$, and a smaller decrease in χ^2/DOF when $n_{\max}$ is further increased to $n_{\max} = 3$. Such a decrease in the χ^2/DOF ratio is even less statistically relevant if we take into account the oscillations in the value of χ^2/DOF due to the uncertainty in U_c and ν. Moreover, the fitted values for $n_{\max} = 2$ and $n_{\max} = 3$ are in agreement with each other, suggesting that within the statistical accuracy a Taylor expansion with $n_{\max} = 2$ is sufficient to describe the data. We also observe that the main contribution to the error bars is due to the uncertainty in U_c and ν.

In line with the findings of Table III, even considering the maximum oscillation of χ^2/DOF upon variation of U_c and ν within one error bar as quoted in Eqs. (27) and (28), all of the fits have a large χ^2/DOF. This confirms the importance of scaling corrections. To monitor their role, we repeat the fits including a scaling correction in the form of a background term, [see Eq. (24)]. To this end, we use

$$\chi(U, L) = L^{1-\eta'} \sum_{n=0}^{n_{\max}} a_n (U - U_c)^n L^{n/\nu}$$
$$+ \sum_{m=0}^{m_{\max}} b_m (U - U_c)^m. \qquad \text{(B2)}$$

Fit results for $n_{\max} = 2$ and three values of $m_{\max}$ are shown in Table X. Upon increasing $m_{\max}$ from $m_{\max} = 0$ to $m_{\max} = 1$, we observe a decrease in the χ^2/DOF ratio that is, however, less significant if we consider the oscillation in the value of χ^2/DOF due to the uncertainty in U_c and ν. A further increase of $m_{\max}$ to $m_{\max} = 2$ does not significantly change the χ^2/DOF ratio. Accordingly, the expansion with $n_{\max} = 2$, $m_{\max} = 1$ should adequately describe the data. The corresponding fits exhibit a small χ^2/DOF for $L_{\min} = 9$, and the resulting value of $\eta' = 0.83(12)$ is in agreement with the estimate of Eq. (25). Moreover, this value agrees with the fit for $L_{\min} = 6$, and also with the fits obtained by setting $n_{\max} = m_{\max} = 2$.

[1] S. Sachdev, *Quantum Phase Transitions*, 2nd ed. (Cambridge University Press, Cambridge, 2011).

[2] M. A. Metlitski and S. Sachdev, *Quantum phase transitions of metals in two spatial dimensions. I. Ising-nematic order*, Phys. Rev. B **82**, 075127 (2010).

[3] M. A. Metlitski and S. Sachdev, *Quantum phase transitions of metals in two spatial dimensions. II. Spin density wave order*, Phys. Rev. B **82**, 075128 (2010).

[4] I. F. Herbut, *Interactions and phase transitions on graphene's honeycomb lattice*, Phys. Rev. Lett. **97**, 146401 (2006).

[5] M. Vojta, Y. Zhang, and S. Sachdev, *Quantum Phase Transitions in d-Wave Superconductors*, Phys. Rev. Lett. **85**, 4940 (2000).

[6] E.-G. Moon, C. Xu, Y. B. Kim, and L. Balents, *Non-Fermi-Liquid and Topological States with Strong Spin-Orbit Coupling*, Phys. Rev. Lett. **111**, 206401 (2013).

[7] I. F. Herbut and L. Janssen, *Topological Mott Insulator in Three-Dimensional Systems with Quadratic Band Touching*, Phys. Rev. Lett. **113**, 106401 (2014).

[8] S. Sorella and E. Tosatti, *Semi-metal-insulator transition of the*

Hubbard model in the honeycomb lattice, Europhys. Lett. **19**, 699 (1992).

[9] T. Paiva, R. T. Scalettar, W. Zheng, R. R. P. Singh, and J. Oitmaa, *Ground-state and finite-temperature signatures of quantum phase transitions in the half-filled Hubbard model on a honeycomb lattice*, Phys. Rev. B **72**, 085123 (2005).

[10] Z. Y. Meng, T. C. Lang, S. Wessel, F. F. Assaad, and A. Muramatsu, *Quantum spin-liquid emerging in two-dimensional correlated Dirac fermions*, Nature **464**, 847 (2010).

[11] C. Xu, *Quantum spin Hall, triplet superconductor, and topological liquids on the honeycomb lattice*, Phys. Rev. B **83**, 024408 (2011); C. Griset and C. Xu, *Phase diagram of the Kane-Mele-Hubbard model*, *ibid.* **85**, 045123 (2012).

[12] S. Sorella, Y. Otsuka, and S. Yunoki, *Absence of a Spin Liquid Phase in the Hubbard Model on the Honeycomb Lattice*, Sci. Rep. **2**, 992 (2012).

[13] F. F. Assaad and I. F. Herbut, *Pinning the Order: The Nature of Quantum Criticality in the Hubbard Model on Honeycomb Lattice*, Phys. Rev. X **3**, 031010 (2013).

[14] C.-C. Chang and R. T. Scalettar, *Quantum Disordered Phase near the Mott Transition in the Staggered-Flux Hubbard Model on a Square Lattice*, Phys. Rev. Lett. **109**, 026404 (2012).

[15] D. Ixert, F. F. Assaad, and K. P. Schmidt, *Mott physics in the half-filled Hubbard model on a family of vortex-full square lattices*, Phys. Rev. B **90**, 195133 (2014).

[16] I. F. Herbut, V. Juričić, and O. Vafek, *Relativistic Mott criticality in graphene*, Phys. Rev. B **80**, 075432 (2009).

[17] S. Ryu, C. Mudry, C.-Y. Hou, and C. Chamon, *Masses in graphenelike two-dimensional electronic systems: Topological defects in order parameters and their fractional exchange statistics*, Phys. Rev. B **80**, 205319 (2009).

[18] H.-Y. Yang, A. F. Albuquerque, S. Capponi, A. M. Läuchli, and K. P. Schmidt, *Effective spin couplings in the Mott insulator of the honeycomb lattice Hubbard model*, New Journal of Physics **14**, 115027 (2012).

[19] L. Wang, P. Corboz, and M. Troyer, *Fermionic quantum critical point of spinless fermions on a honeycomb lattice*, New Journal of Physics **16**, 103008 (2014).

[20] Z.-X. Li, Y.-F. Jiang, and H. Yao, *Solving fermion sign problem in quantum Monte Carlo by Majorana representation*, ArXiv e-prints (2014), arXiv:1408.2269 [cond-mat.str-el].

[21] S. Chandrasekharan and A. Li, *Quantum critical behavior in three dimensional lattice Gross-Neveu models*, Phys. Rev. D **88**, 021701 (2013).

[22] S. Rachel and K. Le Hur, *Topological insulators and Mott physics from the Hubbard interaction*, Phys. Rev. B **82**, 075106 (2010).

[23] M. Hohenadler, T. C. Lang, and F. F. Assaad, *Correlation Effects in Quantum Spin-Hall Insulators: A Quantum Monte Carlo Study*, Phys. Rev. Lett. **106**, 100403 (2011); **109**, 229902(E) (2012).

[24] M. Hohenadler, Z. Y. Meng, T. C. Lang, S. Wessel, A. Muramatsu, and F. F. Assaad, *Quantum phase transitions in the Kane-Mele-Hubbard model*, Phys. Rev. B **85**, 115132 (2012).

[25] D.-H. Lee, *Effects of Interaction on Quantum Spin Hall Insulators*, Phys. Rev. Lett. **107**, 166806 (2011).

[26] C. L. Kane and E. J. Mele, *Quantum Spin Hall Effect in Graphene*, Phys. Rev. Lett. **95**, 226801 (2005).

[27] F. D. M. Haldane, *Model for a Quantum Hall Effect without Landau Levels: Condensed-Matter Realization of the "Parity Anomaly"*, Phys. Rev. Lett. **61**, 2015 (1988).

[28] I. Affleck and J. B. Marston, *Large-n limit of the Heisenberg-Hubbard model: Implications for high-T_c superconductors*, Phys. Rev. B **37**, 3774 (1988).

[29] F. F. Assaad, *Phase diagram of the half-filled two-dimensional $SU(N)$ Hubbard-Heisenberg model: a quantum Monte Carlo study*, Phys. Rev. B **71**, 075103 (2005).

[30] M. Hohenadler, F. Parisen Toldin, I. F. Herbut, and F. F. Assaad, *Phase diagram of the Kane-Mele-Coulomb model*, Phys. Rev. B **90**, 085146 (2014).

[31] I. F. Herbut, V. Juričić, and B. Roy, *Theory of interacting electrons on the honeycomb lattice*, Phys. Rev. B **79**, 085116 (2009).

[32] C. L. Kane and E. J. Mele, *Z_2 Topological Order and the Quantum Spin Hall Effect*, Phys. Rev. Lett. **95**, 146802 (2005).

[33] D. Zheng, G.-M. Zhang, and C. Wu, *Particle-hole symmetry and interaction effects in the Kane-Mele-Hubbard model*, Phys. Rev. B **84**, 205121 (2011).

[34] M. Hohenadler and F. F. Assaad, *Correlation effects in two-dimensional topological insulators*, J. Phys.: Condens. Matter **25**, 143201 (2013).

[35] M. Barber, *Finite-size scaling*, in *Phase Transitions and Critical Phenomena*, Vol. 8, edited by C. Domb and J. Lebowitz (Academic Press, London, 1983) pp. 145 – 266.

[36] J. Cardy, ed., *Finite-Size Scaling*, Current Physics - Sources and Comments (Elsevier Science, North-Holland, 1988).

[37] V. Privman, ed., *Finite Size Scaling and Numerical Simulation of Statistical Systems* (World Scientific, Singapore, 1990).

[38] A. Pelissetto and E. Vicari, *Critical phenomena and renormalization-group theory*, Physics Reports **368**, 549 (2002).

[39] M. Campostrini, A. Pelissetto, and E. Vicari, *Finite-size scaling at quantum transitions*, Phys. Rev. B **89**, 094516 (2014).

[40] A. Aharony and M. E. Fisher, *Nonlinear scaling fields and corrections to scaling near criticality*, Phys. Rev. B **27**, 4394 (1983).

[41] F. Assaad and H. Evertz, *World-line and Determinantal Quantum Monte Carlo Methods for Spins, Phonons and Electrons*, in *Computational Many-Particle Physics*, Lecture Notes in Physics, Vol. 739, edited by H. Fehske, R. Schneider, and A. Weiße (Springer, Berlin Heidelberg, 2008) pp. 277–356.

[42] L. Janssen and I. F. Herbut, *Antiferromagnetic critical point on graphene's honeycomb lattice: A functional renormalization group approach*, Phys. Rev. B **89**, 205403 (2014).

[43] M. Hasenbusch, F. Parisen Toldin, A. Pelissetto, and E. Vicari, *The universality class of 3D site-diluted and bond-diluted Ising systems*, Journal of Statistical Mechanics: Theory and Experiment **2007**, P02016 (2007).

[44] F. Parisen Toldin, A. Pelissetto, and E. Vicari, *Strong-Disorder Paramagnetic-Ferromagnetic Fixed Point in the Square-Lattice $\pm J$ Ising Model*, J. Stat. Phys. **135**, 1039 (2009).

[45] M. Campostrini, M. Hasenbusch, A. Pelissetto, and E. Vicari, *Theoretical estimates of the critical exponents of the superfluid transition in ^{4}He by lattice methods*, Phys. Rev. B **74**, 144506 (2006).

[46] I. F. Herbut, *Quantum Critical Points with the Coulomb Interaction and the Dynamical Exponent: When and Why $z = 1$*, Phys. Rev. Lett. **87**, 137004 (2001).

[47] M. Campostrini, A. Pelissetto, P. Rossi, and E. Vicari, *Strong-coupling analysis of two-dimensional O(N) σ models with $N \geq 3$ on square, triangular, and honeycomb lattices*, Phys. Rev. D **54**, 1782 (1996).